

# Basic hydrodynamics of Richtmyer-Meshkov-type growth and oscillations in the ICF-relevant conditions

BY Y. AGLITSKIY<sup>1,2</sup>, A. L. VELIKOVICH<sup>2</sup>, M. KARASIK<sup>2</sup>, N. METZLER<sup>3,4</sup>, S. ZALESKAK,<sup>2</sup>  
A. J. SCHMITT<sup>2</sup>, L. PHILLIPS<sup>5</sup>, J. H. GARDNER<sup>6</sup>, V. SERLIN<sup>2</sup>, J. WEAVER<sup>2</sup> &  
S. P. OBENSCHAIN<sup>2</sup>

<sup>1</sup>*Science Applications International Corporation, McLean, Virginia 22150*

<sup>2</sup>*Plasma Physics Division, Naval Research Laboratory, Washington, DC 20375*

<sup>3</sup>*ARTEP Inc., Ellicott City, Maryland 21042*

<sup>4</sup>*Department of Mechanical Engineering, Ben Gurion University, Beer Sheva, Israel*

<sup>5</sup>*Laboratory for Computational Physics & Fluid Dynamics, Naval Research Laboratory,  
Washington, DC 20375*

<sup>6</sup>*Berkeley Research Associates, Beltsville, Maryland 20705*

In inertial confinement fusion (ICF), the possibility of ignition or high energy gain is largely determined by our ability to control the Rayleigh-Taylor (RT) instability growth in the target. The exponentially amplified RT perturbation eigenmodes are formed from all sources of the target and radiation non-uniformity in a process called seeding. This process involves a variety of physical mechanisms which are somewhat similar to the classical Richtmyer-Meshkov (RM) instability (in particular, most of them are active in the absence of acceleration), but differ from it in many ways. In the last decade, the radiographic diagnostic techniques have been developed that made direct observations of the RM-type effects in the ICF-relevant conditions possible. New experiments stimulated the advancement of the theory of the RM-type processes. The progress in the experimental and theoretical studies of such phenomena as classical RM instability in finite-thickness targets, re-shock and re-rarefaction of the RM-unstable material interfaces, ablative RM instability, feedout, and perturbation development associated with impulsive loading is reviewed.

**Keywords:** inertial confinement fusion, hydrodynamic instability, Richtmyer-Meshkov instability, shock wave, expansion wave

## 1. Introduction

Interfacial instabilities, such as Rayleigh-Taylor (RT) (Rayleigh 1883, Taylor 1950) and Richtmyer-Meshkov (RM) (Richtmyer 1960, Meshkov 1969), and turbulent mixing driven by these instabilities are ubiquitous in nature. Their manifestations range from a boiling tea kettle in the kitchen to Gulf Stream in the ocean to exploding supernovae (Schmidt 2006). Studies of instabilities and mixing have become one of the most actively developed areas of fluid dynamics. Rapid advancement in flow diagnostics provided a vast amount of data from numerous experiments with liquids and gases on channel, falling- or accelerated-tank facilities and shock tubes, see Niederhaus & Jacobs 2003, Holder *et al.* 2003, Sadot *et al.* 2005, Chapman & Jacobs 2006, Mueschke *et al.* 2006, Dimonte *et al.* 2007, Motl *et al.* 2007, Orlov & Abarzhi 2007, Kumar *et al.* 2007, Schwaederle *et al.* 2007, Wilkinson & Jacobs 2007, Scase *et al.* 2008, and references

Report Documentation Page				Form Approved OMB No. 0704-0188	
Public reporting burden for the collection of information is estimated to average 1 hour per response, including the time for reviewing instructions, searching existing data sources, gathering and maintaining the data needed, and completing and reviewing the collection of information. Send comments regarding this burden estimate or any other aspect of this collection of information, including suggestions for reducing this burden, to Washington Headquarters Services, Directorate for Information Operations and Reports, 1215 Jefferson Davis Highway, Suite 1204, Arlington VA 22202-4302. Respondents should be aware that notwithstanding any other provision of law, no person shall be subject to a penalty for failing to comply with a collection of information if it does not display a currently valid OMB control number.					
1. REPORT DATE <b>2010</b>		2. REPORT TYPE		3. DATES COVERED <b>00-00-2010 to 00-00-2010</b>	
4. TITLE AND SUBTITLE <b>Basic hydrodynamics of Richtmyer-Meshkov-type growth and oscillations in the ICF-relevant conditions</b>				5a. CONTRACT NUMBER	
				5b. GRANT NUMBER	
				5c. PROGRAM ELEMENT NUMBER	
6. AUTHOR(S)				5d. PROJECT NUMBER	
				5e. TASK NUMBER	
				5f. WORK UNIT NUMBER	
7. PERFORMING ORGANIZATION NAME(S) AND ADDRESS(ES) <b>Naval Research Laboratory, Plasma Physics Division,,4555 Overlook Avenue SW, Washington, DC, 20375</b>				8. PERFORMING ORGANIZATION REPORT NUMBER	
9. SPONSORING/MONITORING AGENCY NAME(S) AND ADDRESS(ES)				10. SPONSOR/MONITOR'S ACRONYM(S)	
				11. SPONSOR/MONITOR'S REPORT NUMBER(S)	
12. DISTRIBUTION/AVAILABILITY STATEMENT <b>Approved for public release; distribution unlimited</b>					
13. SUPPLEMENTARY NOTES <b>preprint of an article published by Philosophical Transactions of the Royal Society A.</b>					
14. ABSTRACT					
15. SUBJECT TERMS					
16. SECURITY CLASSIFICATION OF:			17. LIMITATION OF ABSTRACT <b>Same as Report (SAR)</b>	18. NUMBER OF PAGES <b>30</b>	19a. NAME OF RESPONSIBLE PERSON
a. REPORT <b>unclassified</b>	b. ABSTRACT <b>unclassified</b>	c. THIS PAGE <b>unclassified</b>			

therein. Progress in massively parallel numerical simulations (Cabot & Cook 2006), as well as advancements in the theory greatly improved the general understanding of mixing. The physical mechanisms responsible for the perturbation growth and turbulent mixing in shock tubes, channel facilities and imploding laser fusion pellets are similar in many ways, which is why the knowledge gained in the room-temperature experiments proved helpful for the inertial confinement fusion (ICF), guiding the target design and facilitating the data analysis.

At the same time, understanding of many issues related to the perturbation growth and mixing in the ICF targets requires experimental, theoretical and computational studies performed specifically for the ICF-relevant conditions, in high-energy-density (HED) plasmas at or above solid-state density, heated to temperatures from eV to keV and compressed to multi-Mbar pressures. Implosions of ICF capsules include processes and regimes, which are hard or even impossible to emulate in a different environment, such as complex history of acceleration and deceleration of its shell(s) and interface(s), their multiple re-shocks and re-rarefactions (Lindl 1998, Bodner *et al.* 1998, Atzeni & Meyer-ter-Vehn 2004, Pfalzner 2006). Much of the perturbation seeding and growth in such targets occur at the ablation fronts, which can only be produced by interaction of intense radiation or hot plasma with solid matter and whose properties are very different from those of material interfaces.

Although the HED plasmas are a challenging environment for observing hydrodynamic instabilities, some of the relevant basic hydro phenomena, particularly the RM instability growth and related effects, are actually easier to observe and analyze in the ICF/HED plasma experiments. Here are some examples.

1) There is a clear advantage in experimenting with clean, well-characterized rippled interfaces separating two different solid materials. A solid target can remain at rest until shocked (Dimonte & Remington 1993, Dimonte *et al.* 1996, Glendinning *et al.* 2003, Aglitskiy *et al.* 2006). In conventional shock-tube experiments with two gases, the presence of thin membrane affects the early-time perturbation growth. Since the original work of Meshkov 1969 up to the most recent publications (Erez *et al.* 2000, Mariani *et al.* 2008) this “membrane effect” proved to be difficult to eliminate or accurately account for.

2) The rarefaction-triggered counterpart of the RM instability, developing when a rarefaction wave reaches a material interface from a high-density side, has been theoretically discovered long ago (Li & Book 1991, Li *et al.* 1991) and is undoubtedly important for ICF. No room-temperature facility is available for its experimental study. In an ICF experiment, launching a rarefaction wave is easy, it happens naturally when a radiation-driven shock wave breaks out at the rear surface of the target, as in Smitherman *et al.* 1999, Shigemori *et al.* 2000, Aglitskiy *et al.* 2001b, 2006.

3) Most important manifestation of the perturbation growth in a radially imploded ICF target is the lateral mass redistribution inside it that reduces the target uniformity and thus degrades the fusion neutron yield. This process, which is hard to study in room-temperature experiments, is routinely observed in the ICF-relevant conditions, which is made possible by advanced x-ray radiographic diagnostic techniques.

The RM-type hydrodynamic processes, besides the classical RM instability, include a variety of related phenomena, some of which are specific to the ICF targets,

while the other are of more general nature. We focus on the basic physical mechanisms responsible for the onset and early-time, small-amplitude perturbation evolution. This is because the interest to the RM-type processes in the ICF is determined by their role in the RT “seeding,” i. e., formation of the RT eigenmodes, which are subsequently amplified by the exponential RT growth, from the initial target imperfections and radiation non-uniformities. No effort is spared to make the ICF targets and the radiation fields as smooth as possible, so the initial amplitudes of all the Fourier modes representing their non-uniformity are very small. Many of the RM-type processes are oscillatory and can cause only limited growth of initial perturbation growth. The other, like the classical RM instability, can cause large growth, but the ICF target designs and implosion scenarios typically ensure that any RM-type growth is limited to one order of magnitude or so before the RT growth begins.

For this reason, the small-amplitude RT seeding is hard to observe directly and notoriously difficult to model numerically, see Zalesak *et al.* 2005. Until very recently, little experimental data were available for testing the codes and theories in the RT-seeding relevant regimes. The situation changed with the development of new diagnostic techniques (Aglitskiy *et al.* 2001a, 2001b, 2002, 2006, Gotchev *et al.* 2006), which made it possible to study the whole array of the previously unexplored RM-type processes in the ICF targets.

In this article we summarize the results of such studies performed over the last decade, mainly at the Naval Research Laboratory (NRL) and based on direct observations, most of which have been done for the first time. In Section 2 we review the drivers and diagnostic capabilities available for ICF-HEDP experiments on RM-type instabilities. In Section 3 we discuss the so-called ablative RM instability which approximates the limiting case of Atwood number  $A = 1$  of the classical light-to-heavy RM instability, when a rippled ablation front is simultaneously produced and shocked by a laser or x-ray radiation rapidly turned on. Section 4 is dedicated to the opposite limiting case of the classical heavy-to-light RM instability  $A = -1$ , the feedout situation, when the shock wave arrives to a rippled rear surface of a target, behind which there is no low-density material. In Section 5 we describe the effect of a re-shock, which stops the acceleration of a RT unstable ablation front and quenches the RT growth. In Section 6 we discuss the perturbation evolution in a shock-rarefaction flow produced by impulsive loading: A short powerful laser pulse that is turned off immediately after depositing a finite energy on a rippled target surface. In Section 7 we conclude with a discussion.

## **2. Laser drivers and diagnostics**

The ICF-relevant high energy density parameter range for hydrodynamic experiments means multi-Mbar pressures (Lindl 1998, Atzeni & Meyer-ter-Vehn 2004, Pfalzner 2006.) This is the pressure range required for strong shock compression of solid targets, see Zel’dovich & Raizer 2002, Chapter XI. The multi-Mbar pressure needs to be maintained for a sufficiently long time, over a sufficiently wide area to produce the required 1D flow and observe the perturbation development characteristic of it. These conditions determine the requirements on laser drivers suitable for the relevant experiments.

The ablative pressure produced by direct laser irradiation of a solid deuterium or plastic target can be estimated as

$$p \cong \left( \frac{I}{\lambda_L} \right)^{2/3} \left( \frac{m_u}{r_e} \right)^{1/3} = 0.4 \times \left[ \frac{I (\text{TW/cm}^2)}{\lambda_L (\mu\text{m})} \right]^{2/3} \text{ Mbar}, \quad (1)$$

where  $I$  and  $\lambda_L$  are the laser intensity and wavelength, respectively,  $m_u$  is the atomic mass unit and  $r_e$  is the classical electron radius, see Manheimer *et al.* 1982. For indirect soft x-ray drive, the ablative pressure in the hohlraum cavity is related to its radiation temperature  $T_r$  by

$$p \cong 3 \times 10^{-7} \times [T_r (\text{eV})]^{7/2} \text{ Mbar}, \quad (2)$$

see Lindl 1998. Laser-produced pressure of  $p = 10$  Mbar corresponds to the intensity  $I$  ranging from 31 TW/cm<sup>2</sup> to 66 TW/cm<sup>2</sup> for laser wavelength varied from 0.248  $\mu\text{m}$  (KrF laser) to 0.53  $\mu\text{m}$  (second harmonic of Nd-glass laser radiation). The hohlraum temperature required to produce the same pressure is 140 eV.

Table I presents the parameter range for the RM-type hydrodynamic experiments performed so far in the ICF-relevant conditions. It is relatively narrow: driving pressure  $p$  from 7 to 45 Mbar, laser pulse duration  $t_L$  from 1.5 to 11 ns, shock velocity  $D$  from 20 to 60  $\mu\text{m/ns}$ , payload diameter from 300 to 800  $\mu\text{m}$ , ripple wavelength  $\lambda$  from 20 to 150  $\mu\text{m}$ . Indeed, estimating  $D \cong \sqrt{p/\rho}$ , we find that a  $\sim 10$  Mbar pressure drives a shock wave into a solid plastic or a light metal ablator like Be (Dimonte & Remington 1993) or Al (Smitherman *et al.* 1999) at the velocity  $\sim 2 - 3 \times 10^6 = 20 - 30$   $\mu\text{m/ns}$ . To make the RM-type phenomena observable, the driving pressure in most cases needs to be maintained while the shock propagates more than one ripple wavelength  $\lambda$ . This imposes a lower limit on the duration of the pressure drive. On the other hand, the accelerated area should be wide enough to cover a large number of wavelengths  $\lambda$ , to ensure periodicity. These two conditions require high laser energy delivered to the target on a ns time scale. In direct-drive experiments, like those reported by Aglitskiy *et al.*, 2001a, 2001b, 2002, 2006, Glendinning *et al.* 2003, Weaver *et al.*, 2004, Gotchev *et al.*, 2006, about 0.5-2.5 kJ of laser energy needs to be deposited into the focal spot. For soft x-ray drive experiments, laser energy of 20-30 kJ has to be delivered into the hohlraum, because the ablator pushing the payload can constitute only a small fraction of its wall area (Dimonte & Remington 1993, Dimonte *et al.* 1996).

Only high-power, high energy, multi-beam laser systems developed for the ICF can satisfy these requirements. The 10-beam, 40-kJ NOVA laser at the Lawrence Livermore National Laboratory (LLNL) had been shut down in 1999, but all the other drivers listed in Table I remain in operation: the 12-beam GEKKO-XII/HIPER laser facility at the Institute of Laser Engineering, Osaka University, Japan (2.4 kJ in 0.351  $\mu\text{m}$  wavelength radiation, see Yamanaka 1985), the 60-beam OMEGA laser facility at the Laboratory for Laser Energetics, University of Rochester (30 kJ in 0.351  $\mu\text{m}$ , see Boehly *et al.* 1995) and the 56-beam Nike KrF laser facility at the Naval Research Laboratory (3 kJ in 0.248  $\mu\text{m}$ , see Obenschain *et al.* 1996).

Next-generation high energy lasers are presently being built, opening new opportunities for hydrodynamic experiments. Construction of the 196-beam, 1.8 MJ in 0.351  $\mu\text{m}$  National Ignition Facility (NIF) at LLNL has been completed in March 2009. A similar ignition-scale facility Laser Megajoule (LMJ, 240 beams, 1.8 MJ in 0.351  $\mu\text{m}$ ) is under construction at CESTA, France (Besnard 2007). A 4-beam, 10 kJ in 0.351  $\mu\text{m}$  LMJ prototype, Ligne d'Intégration Laser operates in France since 2002 (Eyharts *et al.* 2006). A 8-beam, 15-20 kJ in 0.351  $\mu\text{m}$  glass laser system operates in China since 2005 as a prototype of the 64-beam, 150-200 kJ Shenguang-III facility (He & Zhang 2007). A 4-beam, 9 kJ in 0.351  $\mu\text{m}$  glass laser system Luch is under construction at VNIIEF, Russia (one of its beams is operational since 2002, see Garanin *et al.* 2005) as a prototype of the 128-beam, 300 kJ Iskra-6 facility.

**Table I.** Parameters of the RM-type hydrodynamic experiments on high energy laser facilities. Here  $\lambda_L$  and  $t_L$  are laser wavelength and pulse duration, respectively,  $p$  is the pressure maintained by the driver,  $\varnothing$  is the diameter of the laser- or soft-x-ray driven area,  $D$  is the velocity of the shock wave driven into the target,  $\lambda$  is the ripple wavelength,  $h\nu$  is the photons energy of backlighting x rays, with backlighter material indicated.

Driver	$\lambda_L$ , $\mu\text{m}$	$p$ , Mbar	$t_L$ , ns	$\varnothing$ , $\mu\text{m}$	$D$ , $\mu\text{m}/\text{ns}$	$\lambda$ , $\mu\text{m}$	$h\nu$ , keV material	Experiment	Reference
NOVA (LLNL)	0.53	15, 30	3	850	30-50	100	2-3 Mo 5-6 Fe	Classical RMI	Dimonte & Reminton 1993, Dimonte <i>et al.</i> 1996
		7, 15	2.2, 4.5	800	20-30	50	4.3-6.7 Ti 6.7-8.3 V	Feedout	Smitherman <i>et al.</i> 1999
GEKKO-XII (ILE)	0.53	9	2.2	300	35	60, 100	1.6-1.8 Ge 2.5-2.9 Mo	Rippled shock oscillations	Endo <i>et al.</i> 1995
		9	2.3	600	34	100	1.15-1.3 Cu	Feedout	Shigemori <i>et al.</i> 2000
Nike (NRL)	0.248	8-13	4	400	40	30, 45	1.85 Si monochrom.	Ablative RMI, feedout, classical RMI, impulsive loading, re-shock	Aglitskiy <i>et al.</i> 2001a, 2001b, 2002, 2006, Weaver <i>et al.</i> 2004
OMEGA (LLE)	0.351	7	11	800	20	150	~4.3 Sc	Classical RMI	Glendinning <i>et al.</i> 2003
		45	1.5	700	60	20, 30	1.4-1.56 U	Ablative RMI	Gotchev <i>et al.</i> 2006

The RM-type hydrodynamic effects involve redistribution of mass in cold and dense areas of laser-driven targets. Such mass motions are observed directly using absorption of hard x rays as a diagnostic tool. For this, a powerful external source of x rays is needed to illuminate the target, and an imaging system – to record the distribution of mass probed by the x rays. The ICF x-ray sources are backlighters – small targets made of high-atomic-number materials, which are irradiated by the separate laser driver's beams to convert laser energy into keV x-ray radiation. Table I lists the backlighter materials and the corresponding energies of the x-ray photons used in the RM-type

experiments. To ensure that the hard x-ray source is bright enough to probe thick, dense targets, experiments often require a large amount of laser energy for backlighting – about as much as is used to drive the target (Gotchev *et al.* 2006) or even more (Dimonte & Remington 1993, Dimonte *et al.* 1996, Glendinning *et al.* 2003).

For any backlighting scheme there are two desirable features of the imaging system: smaller size of the backlighter source and filtration of the imaging radiation from the self-emission of the object. If the dimension of the source of backlighting radiation is small, the laser power required to create it can be much smaller than the power driving the object. If spectral filtration is available, the surface brightness of backlighter must be larger than the object brightness only in the bandwidth of the spectral line being used to image the object. The large spot size of the main driver is necessary to minimize the edge effects from the acceleration process and therefore requires a diagnostic field of view of approximately 1 mm, so that the entire focal spot as well as the remaining intact part of the target foil are within the picture.

A monochromatic x-ray imaging system based on Bragg reflection from spherically curved crystals (Brown *et al.* 1997a) has been successfully used on the NRL KrF Nike laser to observe the evolution of target mass perturbations. Compared to other x-ray imaging techniques like pinholes, Kirkpatrick-Baez microscopes, and Fresnel lenses, a curved crystal imager has several advantages. It is a high throughput, high spatial resolution, and, by nature, monochromatic diagnostic technique with a large field of view, all at the same time.

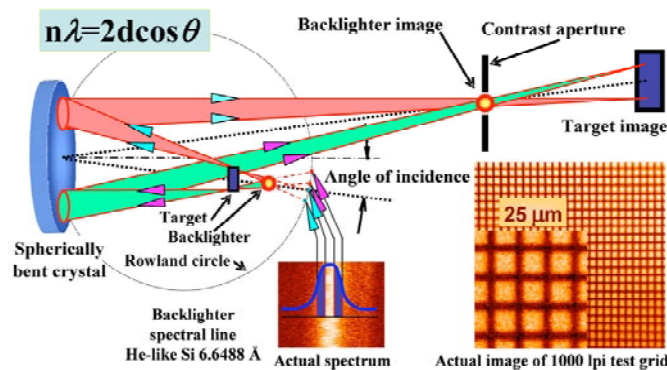


**Figure 1.** The general scheme of the monochromatic x-ray imaging diagnostics fielded on Nike laser. Also shown: the shape of a Si backlighter spectral line and test images obtained on x-ray film (magnified in the inset).

The optical scheme of monochromatic x-ray backlighting (Rode *et al.* 1990, Pikuz, S. A. *et al.* 1995a, 1995b, 1997, Pikuz, T. A. *et al.* 1995, Aglitskiy *et al.* 1996, Brown *et al.* 1997a, 1997b, Sanchez del Rio *et al.* 1997, Pawley *et al.* 1997) is presented in Fig. 1. Imaging of just top and bottom points of the main target is shown. For the scheme description we use here the well known Rowland circle, which is a curve where all x rays with a given wavelength  $\lambda$  focus to a point. There is no restriction on the source location provided the radiation wavelength  $\lambda$  satisfies the Bragg equation  $2d \sin \theta = m\lambda$ , where  $d$  is the crystal interplanar distance,  $m$  - the order of reflection, and  $\theta$  - the Bragg (grazing) angle.

The x-ray backlighter source is located between the main target and the Rowland circle of radius  $R/2$ , where  $R$  is the curvature radius of the crystal. When a small x-ray source backlights a specific point of the object, the area of the crystal involved in the imaging of this point is much smaller (0.5-1 mm) than the crystal itself. Due to the focusing of the backlighter radiation source between the crystal and the object image, it is possible to protect the detector from a significant portion of the self-radiation of the object being imaged. Initially, the curved crystal imager has been used at NRL in combination with a framing camera to provide sequences of high spatial resolution still images (up to four snapshots that correspond to four different times) taken with a time resolution of 200 ps (Brown *et al.* 1997b). This diagnostic technique is fully adequate when the observed mass non-uniformity varies monotonically in time, e. g., during the fast RT growth (Brown *et al.* 1997b, Sanchez del Rio *et al.* 1997).

Observation of essentially non-monotonic evolution of the processes under study like the oscillatory ablative RM instability, presents a new challenge to the imaging diagnostics. With areal mass modulation amplitude oscillating in time, the diagnostics that record a limited number of images incrementally over a relatively long period of time are difficult to apply: it is easy to lose important information or even completely miss the effect. To extend the capabilities of our diagnostic technique, we modified the Nike imaging diagnostic setup by adding a streak camera to the system, which made it possible to analyze continuous time behavior of the x-ray images.

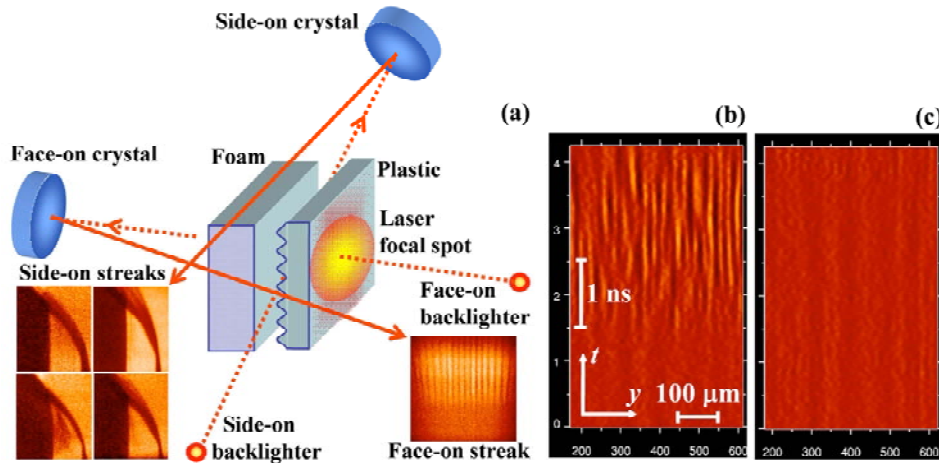


**Figure 2.** (a) Orthogonal x-ray imaging diagnostics implemented on Nike laser. Face-on and side-on images are formed by two separate backlighters and spherically bent crystals. For a rippled double-foil target shown in the figure, the side-on streak records (left) shows the time history of collision, and the face-on streak record (right) – the perturbation evolution. (b), (c) Face-on streak records of a single 30  $\mu\text{m}$  thick smooth target driven by a 4 ns Nike pulse with a foot: (b) pure plastic target, (c) plastic target covered with a 450 Å gold layer.

The diagnostic setup is presented in Fig. 2(a). Approximately 500 J is delivered to one or two silicon backlighter targets, producing x-rays that backlight the main target for about 5 ns. The spherically curved quartz crystal with the cut 1011 and radius of curvature of 200 mm selects the resonance line of the He-like Si (1.86 keV) and projects a monochromatic image of the target on the slit of the x-ray streak camera. Face-on and side-on images are formed by two separate backlighters and spherically bent crystals. The face-on streak record (Fig. 2(a), right) shows the 2D evolution of areal mass perturbations



in the target. The monochromatic x-ray imaging makes it possible to translate the observed modulation of the optical thickness directly into the modulation of the areal mass. Two examples of face-on streak records are shown on Fig. 2(b), (c). The side-on streak records (Fig 2(a), left) show the 1D time history of the CH foil acceleration, plastic-on-foam collision, the propagation of shock waves and the dynamics of the ablation front. The streak records were taken with a time resolution of 170 ps, which is sufficient for the  $\sim 0.5$  ns characteristic times of interest. A somewhat similar setup with a thin slit as an imaging device has been used at NRL for the pioneering measurements of the RT growth rates (Whitlock *et al.* 1987).

To resolve the RM-type effects triggered by the well-defined initial single-mode perturbations in the target (the ripples), it is necessary to ensure that the driving radiation field is sufficiently smooth, and the non-uniformity of the drive is not an issue for the relevant range of perturbation wavelengths. This is the case for indirectly-driven experiments (Dimonte & Remington 1993, Dimonte *et al.* 1996, Smitherman *et al.* 1999). The price paid for high uniformity of the driving soft x-rays in the hohlraum is its low energy efficiency: only  $\sim 10\%$  of the total x-ray energy is delivered to the ablator. On the other hand, if the target is directly driven by the laser radiation, it needs to be smoothed, which is a general requirement for the direct-drive ICF (Bodner *et al.* 1998, Lehmberg & Rothenberg 2000). The ICF glass lasers use smoothing by spectral dispersion (2-D SSD) with distributed phase plate and polarization smoothing utilizing birefringent wedges, see Regan *et al.* 2005 and references therein. For  $N = 10$  OMEGA beams overlapped on the target (Gotchev *et al.* 2006) the 1.77% non-uniformity of a single 1 ns laser pulse at 1 THz SSD bandwidth decreases by a factor of  $\sqrt{N}$  to  $\sigma_{rms} = 0.6\%$ . The KrF Nike laser beams are smoothed using the induced spatial incoherence (ISI) technique, which provides the best beam uniformity that has been achieved so far:  $\sigma_{rms} = 1\%$  for a 4-ns Nike beam at 1 THz bandwidth (Deniz *et al.* 1998). The RM-type hydrodynamic experiments on Nike (Aglitskiy *et al.* 2001a, 2001b, 2002, 2006, Weaver *et al.* 2004) are typically made with 37-40 beams overlapping on the target, which reduces  $\sigma_{rms}$  below 0.25%.

Figures 2(b), (c) demonstrate that even such ultra-uniform illumination does not completely eliminate the laser imprint. They present face-on streak records obtained for 30  $\mu\text{m}$  thick flat CH targets driven by a 4-ns 50 TW/cm<sup>2</sup> Nike pulse with a 1.6 ns, 8 TW/cm<sup>2</sup> foot. One of these targets is pure plastic [Fig. 2(b)], and the front side of the other is covered with a 450 Å layer of gold [Fig. 2(c)]. Both records show no visible non-uniformity up to  $t \approx 1.5$  ns. Within this time interval, the foot of the laser pulse pre-compresses the target, and its acceleration by the main Nike pulse starts at 0.7 ns. The RT instability amplifies the random non-uniformity of the laser irradiation, and by  $t = 2$  ns the plastic target is already severely distorted by the perturbation growth, as evidenced by the streak record. Figure 2(c) shows how the thin gold layer makes the target more imprint-resistant, as discussed by Obenschain *et al.* 2002: no RT growth is observed till the end of the main pulse. To minimize the effect of the random perturbations due to laser imprint, as shown in this example, special measures should be taken in the RM-type hydrodynamic experiments. One needs either to avoid or shorten the acceleration phase, when random laser perturbations are exponentially amplified (this implies the use of thicker targets or laser pulses without a foot) or to use some technique for imprint

mitigation. In particular, in Section 3 we discuss the effect of high-Z layer on the ablative RM instability.

To correctly model the RT growth, we need to answer the following important question: How large is the ablation front ripple amplitude at the moment when the acceleration starts? More generally, how does this amplitude evolve with time during the shock-rarefaction transit, before the ablation front starts to accelerate? Physical mechanisms shaping this evolution are responsible for seeding the exponentially growing RT eigenmodes at the ablation front. Their growth, in turn, limits the fusion energy gain in the target.

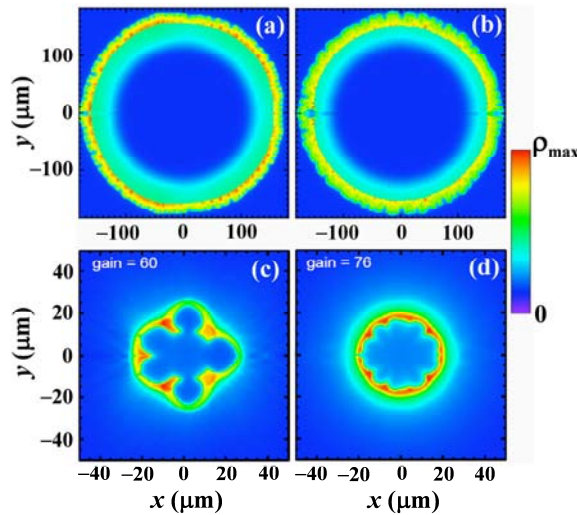


**Figure 3.** RT seeding in a DT-ice target via outer (left) and inner (right) surface roughness. Density maps are shown after the ignitor shock launch (top) and as burn begins (bottom).

This is illustrated by Fig. 3 showing density profiles for an imploding spherical DT target obtained in a high-resolution 2-D simulation (spherical harmonics with  $l$  from 1 to 256 are resolved). The simulation has been done for the shock ignition direct-drive implosion (Betti *et al.*, 2007), which involves a fast re-compression of an expanding central hot spot with a converging shock wave driven by a short, powerful “ignitor” laser pulse irradiating the target at peak compression. The two left frames are simulated for the perturbations seeded by the  $0.49 \mu\text{m}$  rms random non-uniformity of the outer target surface. The right frames correspond to  $1 \mu\text{m}$  rms random non-uniformity of the inner target surface. Different perturbation seeding and development scenarios affect final compression and gain, which is found to be 60 in the former case and 76 in the latter. Of course, separating these contributions to the RT seeding is only possible in the simulations; in the implosions of the ICF targets, all sources of non-uniformity contribute simultaneously. To make sure that simulations describe these seeding mechanisms correctly, we do specially designed experiments where they can be actually separated. These experiments provide data and insight necessary to benchmark the codes and check sanity of their predictions.

### 3. Ablative RM instability

Let us turn on a powerful laser instantly upon a rippled surface of a target. High ablative pressure launches a shock wave into the target. If instead of laser radiation we had instantly applied to the target surface and maintained a constant high pressure, the perturbation evolution would have been completely equivalent to the classical light-to-heavy RM instability, representing its limiting case  $A \rightarrow +1$  (Velikovich *et al.* 1998).

However, stability properties of an ablation front are very different from those of a material interface. The ablation front is stabilized by two distinct physical mechanisms. One of them, first discussed by Bodner 1974, is due to the mass flow through the ablation front. This flow transfers the perturbations from the dense plasma near the ablation front to the low-density plasma corona. There is also another, stronger stabilizing effect. It was discovered theoretically by Sanz 1994, identified and labeled “the rocket effect” by Piriz *et al.* 1997 (see also Piriz 2001). It emerges because, as first noted by Bodner 1974, the ablation front is an isotherm. When it is perturbed, and part of it gets closer to the hot corona, the temperature at this part of the ablation front does not increase, but the temperature gradient in its vicinity,  $\nabla T$ , does. This, in turn, increases the local heat flux from the hot corona to the ablation front,  $-\kappa \nabla T$ , and hence the rate of mass ablation from it, thereby increasing the ablative pressure and producing a restoring force that pushes this part of the ablation front back from the laser absorption zone. The physics of this “rocket effect” is discussed in detail by Piriz *et al.* 1997, Goncharov 1999, Piriz 2001.

With both stabilizing effects taken into account, the growth rate of the ablative RT instability at low acceleration  $g$  (which means high Froude number:  $\text{Fr} = v_a^2 / g L_a \gg 1$ , where  $v_a = \dot{m} / \rho_a$  is the ablation velocity,  $\dot{m}$  is the rate of mass ablation,  $\rho_a$  is the density of the shock-compressed target at the ablation front,  $L_a$  is the density gradient length scale near the ablation front) is given by:

$$\Gamma \cong \left( gk - \frac{1}{r_D} k^2 v_a^2 \right)^{1/2} - 2k v_a \quad (3)$$

(Sanz 1994, Piriz *et al.* 1997, Goncharov *et al.* 1996). Here,  $r_D \ll 1$  is the effective blowoff-plasma-to-ablation front density ratio, a parameter of the sharp boundary model. This parameter is a decreasing function of the ripple wavelength  $\lambda = 2\pi / k$  because perturbation eigenmodes of longer wavelengths extend farther into the low-density corona plasma; its value is estimated using the formulas of Betti *et al.* 1998a. Substituting into (3)  $g = 0$  (no acceleration of the ablation front during the shock/rarefaction transit), we obtain:

$$\Gamma \cong \pm i\Omega - 2k v_a, \quad (4)$$

where  $\Omega = k v_a / \sqrt{r_D}$ .

The complex frequency (4) corresponds to damped oscillations of the ablation front in the absence of acceleration. The imaginary term in (4) describes stabilization of the ablation front by the restoring force due to the “rocket effect” (Piriz *et al.* 1997, Goncharov 1999, Piriz 2001). The real term (exponential decay) expresses the

stabilization due to the mass flow through the ablation front (Bodner 1974). Decaying oscillations of the ablation front have been first detected in simulations (Velikovich *et al.* 1998). The theory of this effect was given, and the term “ablative RM instability” coined by Goncharov 1999. Since the “ablative RM instability” (that is, classical RM instability stabilized by the ablative mechanisms) manifests itself in decaying oscillations, they will also be referred below as ablative RM oscillations.

The oscillations can be directly seen by observing the time evolution of the areal mass modulation amplitude, which is defined as

$$\delta m = \delta \int_0^{\infty} \rho(r, \theta, \varphi) r^2 dr \quad \text{or} \quad \delta m = \delta \int_{-\infty}^{+\infty} \rho(x, y, z) dx \quad (5)$$

for spherical and planar geometry, respectively. Here,  $\delta F$  is the modulation amplitude of the variable  $F$  with respect to variation of the transverse coordinates,  $(\theta, \varphi)$  or  $(y, z)$ . Compared to the displacement amplitude of the ablation front,  $\delta x_a$ , the areal mass modulation amplitude  $\delta m$  is a much more convenient perturbation variable to be estimated from the simulation results and experimental data. The computed value of  $\delta m$  is a result of integration, which smoothes out numerical errors, whereas determination of  $\delta x_a$  requires either numerical differentiation, which is notoriously noisy, or some kind of interface tracking. Experimentally,  $\delta m$  is evaluated from the modulation of the optical thickness, which is directly observable with face-on x-ray radiography. The measurements of  $\delta x_a$  can be made only from side-on observations, which require a very precise alignment and are difficult for short perturbation wavelengths,  $\sim 50 \mu\text{m}$  or less. However, the measured or simulated amplitude  $\delta m$  reflects not only the interfacial growth. Multiple processes and mechanisms of perturbation evolution, of which the interfacial RM-type growth might or might not be the dominant one, contribute to  $\delta m$ . To analyze the experimental data and simulation results on  $\delta m$ , we need to understand the physics behind all these contributions.

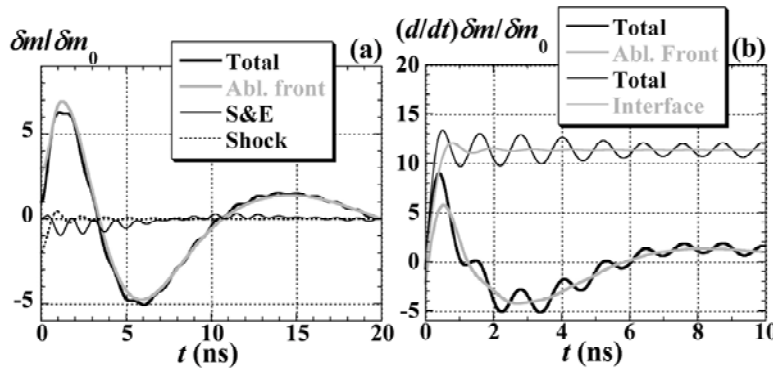


**Figure 4.** Time histories of the normalized areal mass modulation amplitude (a) and its time derivative (b) for the ablative RM instability. Dotted lines in (b) show the corresponding results for classical RM instability growth in the limit  $A = 1$ . Shock velocity  $D = 4 \times 10^6 \text{ cm/s}$ , ablation velocity  $v_a = 10^5 \text{ cm/s}$ , ripple wavelength  $\lambda = 30 \mu\text{m}$ .

Figure 4 shows the oscillations of  $\delta m$  predicted by the small-amplitude sharp boundary model. The total amplitude  $\delta m$  is shown in Fig. 4(a) as a thick black line. The

gray line shows the contribution to it from the ablation front ripple,  $\rho_a \delta x_a$  (where  $\rho_a$  is the plasma density at the ablation front). The contribution to  $\delta m$  from sonic and entropy perturbations are shown as thin solid line labeled S&E, and the contribution from the rippled shock wave – as a dotted line. Figure 4(b) shows time derivatives of  $\delta m$  and  $\rho_a \delta x_a$  as thick black and gray lines, respectively. To emphasize the difference between the ablative and classical RM instability, thin lines in Fig. 4(b) show the same variables for the classical RM case  $A = 1$  when the ablation effects are neglected, all other parameters being the same.

This example has been constructed for the parameters roughly corresponding to the experiments with plastic targets on the Nike laser: shock speed  $D = 4 \times 10^6$  cm/s, shock compression ratio 3, shock pressure 11 Mbar, ablation velocity  $v_a = 10^5$  cm/s, ripple wavelength  $\lambda = 30 \mu\text{m}$ , initial target density  $\rho_0 = 1.07$  g/cm<sup>3</sup>,  $r_D = 0.09$ . This corresponds to the estimated period of the ablation front oscillations  $T = \lambda \sqrt{r_D} / v_a \approx 9$  ns, consistent with Fig. 4(a). The ablative RM rate  $(d/dt)\delta m$  is seen to oscillate around zero, whereas the classical RM growth rate tends to a positive constant found from Wouchuk 2001. The frequency of decaying oscillations of the rippled shock wave transmitted into the target  $\sim kc_s \approx kD$  is  $\sim 10^8$  s<sup>-1</sup>, much higher than that of the ablation front oscillations. Amplitude of these oscillations is seen in Fig. 4(b) to be about the same for the cases of classical and ablative RM instability, which is not surprising: oscillations of a rippled shock wave are weakly coupled to the piston driving the shock. Such oscillations have been first observed in the ICF-relevant conditions by Endo *et al.* 1995 on GEKKO-XII laser. Both face-on x-ray radiography and streaked optical self-emission shock breakout diagnostic indicated a phase reversal of the rippled shock front when the shock propagated  $\sim 0.9\lambda$  into the plastic target. This agrees well with our Fig. 4(a), where the shock travel distance corresponding to the first phase reversal of the rippled shock front equals  $0.85\lambda$ .

Figure 4 demonstrates that after the first 1 ns the contributions both to  $\delta m$  and to  $(d/dt)\delta m$  from the ablation front dominate. Observe, however, that the growth of  $\delta m$  by a factor of  $\sim 7$  shown in Fig. 4(a) is noticeably stronger than the corresponding growth of the ablation front ripple amplitude,  $\delta x_a$ , which increases only by a factor of 2.3. To explain this mismatch, note that at very early time

$$\delta m \approx \rho_a \delta x_a - (\rho_a - \rho_0) \delta x_s, \quad (6)$$

where  $\delta x_s$  is the shock ripple amplitude, and  $\rho_a / \rho_0 = 3$  in this example is the shock compression ratio. When the shock wave is launched,  $\delta x_a = \delta x_s = \delta x_0$ , so that  $\delta m = \rho_0 \delta x_0 = \delta m_0$ . The oscillations of the rippled shock front, however, have a much higher frequency and decay much faster than those of the ablation front. The shock front flattens within 0.6 ns. The ablation front reaches its peak amplitude of  $\delta x_a \approx 2.3 \times \delta x_0$  at about  $t = 1.2$  ns. The resulting peak value of  $\delta m$  is estimated from (6) by neglecting the rippled shock contribution:  $\delta m \approx \rho_a \delta x_a \approx 3\rho_0 \times 2.3\delta x_0 = 6.9\delta m_0$ .

To observe the ablative RM oscillations, the laser pulse duration  $t_L$  must be long enough, the perturbation wavelength  $\lambda$  short enough, and the target thickness  $L$  - large enough, so that the ablative pressure on the target can be maintained for sufficiently long time before it starts to accelerate. With the aid of (4), (6) one can estimate the requirements on  $L$  and  $t_L$  that must be met to observe the first phase reversal, when both the areal mass modulation amplitude,  $\delta m$ , and the ablation ripple amplitude,  $\delta x_c$ , change sign (Aglitskiy *et al.* 2002):

$$L > \frac{2Dr_D^{1/2}\lambda}{9v_a}, \quad t_L > \frac{3L}{2D}. \quad (7)$$

For the conditions of Fig. 4, we obtain from (7):  $L > 80 \mu\text{m}$ ,  $t_L > 3 \text{ ns}$ , in agreement with the figure. If the perturbation wavelength is longer and the laser pulse is shorter, as in the experiments of Endo *et al.* 1995 ( $\lambda = 60$  to  $100 \mu\text{m}$ ,  $L = 40$  to  $80 \mu\text{m}$ ,  $\tau_L = 2.2 \text{ ns}$ ,  $I = 40 \text{ TW/cm}^2$ ,  $\lambda_L = 0.53 \mu\text{m}$ ), the observation time might not be sufficient to see the oscillation of the ablation front. Indeed, the side-on radiography used by Endo *et al.* 1995 did not detect any growth of the ablation front ripples. They correctly attributed the changes in  $\delta m$  observed with face-on radiography to the oscillations of the shock front, which occur on a faster time scale, cf. Fig. 4.

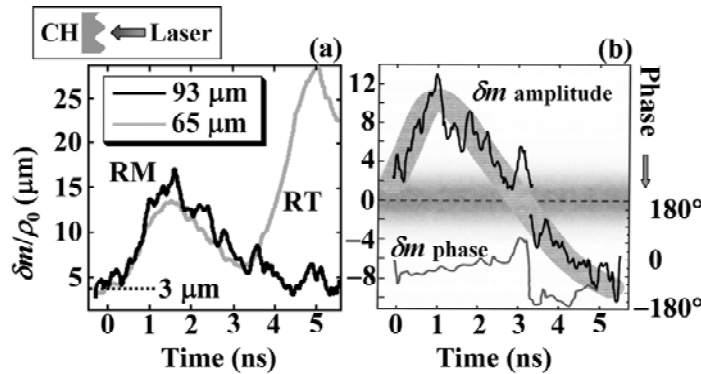


**Figure 5.** (a) Amplitudes of the dominant Fourier mode vs. time for a  $93 \mu\text{m}$  (black) and  $65 \mu\text{m}$  thick (gray) parts of the target; horizontal dotted line shows the initial peak-to-valley amplitude. (b) Amplitude and phase of the dominant Fourier mode for a  $99 \mu\text{m}$  thick target. Thick gray line shows the approximate experimental uncertainty. Phase reversal of  $\delta m$  detected at about  $3.3 \text{ ns}$ . The inset shows schematic of the experiment.

The first direct experimental observations of the ablative RM oscillations have been made on the Nike laser at intensities about  $60 \text{ TW/cm}^2$  and reported by Aglitskiy *et al.* 2001a. They are illustrated by Fig. 5. Here the Fourier-mode amplitude  $\delta m$  is normalized with respect to the initial target density  $\rho_0$  and expressed in  $\mu\text{m}$ . The inset illustrates schematic of the experiment. Figure 5(a) presents the results obtained for a stepped target consisting of two halves,  $65 \mu\text{m}$  and  $93 \mu\text{m}$  thick. The planar front surface of this solid CH target has been rippled at  $\lambda = 45 \mu\text{m}$ , peak-to-valley ripple initial amplitude  $3 \mu\text{m}$ . Since the two halves of this target are driven by the same laser pulse, the stepped target design ensures that the ablative RM oscillations should proceed identically in both halves during the shock-rarefaction transit time. Within the experimental error,

which is larger for the thicker half due to higher attenuation of the backlighting x-rays, this is indeed consistent with the observations. The peak value of  $\delta m \sim 5\delta m_0$  in both cases corresponds to the increase of the ablation front ripple amplitude from the initial value of  $\delta x_0$  by the factor of 1.5 or so. The main contribution to the early-time peak five-fold increase of  $\delta m$  is due to the flattening of the rippled shock front transmitted into the target, as explained above.

The shock-rarefaction transit time is shorter for the thinner half of the stepped target. At about 2.5 ns its acceleration starts, switching the perturbation evolution into the exponential ablative RT growth. In the thicker half of the target, the ablative RM oscillation continues. It approaches a phase reversal of  $\delta m$ , but according to (7), the 4 ns Nike laser pulse duration is not sufficient to observe it at  $\lambda = 45 \mu\text{m}$ . Such phase reversal has been directly observed in a thicker target, 99  $\mu\text{m}$ , rippled from the front surface at shorter wavelength,  $\lambda = 30 \mu\text{m}$ , see Fig. 5(b). Time histories of both amplitude and phase of the areal mass modulation both indicate phase reversal observed at about 3 ns, as in Fig. 6.

These direct observations of the ablative RM oscillations (Aglitskiy 2001a) and of the phase reversal in the target rippled from the front side prior to the start of its acceleration (Aglitskiy 2002) added confidence in our understanding of basic physics of the ablative RM oscillations. To perform a more stringent test of the theory, we need to vary its most significant parameter, the ablation velocity  $v_a$ : The theory predicts that the efficiency of the “rocket effect” stabilizing mechanism responsible for such oscillations becomes more efficient with the increase of  $v_a$ . According to the planar steady-state model of the ablation front, the ablation velocity scales as

$$v_a \propto \rho_a^{-1} \lambda_L^{-14/15}, \quad (8)$$

where  $\lambda_L$  is the laser wavelength (Manheimer *et al.* 1982). For a given laser driver, the straightforward way of increasing the ablation velocity is decreasing the density of the target. Technology of the target fabrication makes it possible now to do experiments with low-density foam targets rippled on the front (Watari *et al.* 2008). It is more instructive, however, to see the effect of ablation velocity increase due to density reduction on the same target as in (Aglitskiy *et al.* 2001a, 2002), in the same shot. It can be achieved by using a target, a part of which is coated with a very thin ( $\sim 1000 \text{ \AA}$ ) layer of a high-Z material, like gold or palladium. Laser radiation absorbed by the high-Z material is immediately converted into x-rays and re-radiated, heating, ablating, and thereby reducing the density of the target’s outer layers, until the high-Z layer expands and becomes transparent. The corresponding increase in  $v_a$  has been demonstrated to strongly mitigate the ablative RT instability (Obenschain *et al.* 2002). We have directly observed its effect on the ablative RM oscillations.

Figure 6 compares observed and simulated amplitude of the dominant Fourier mode vs. time for the uncoated and coated with a 800  $\text{\AA}$  Pd layer halves of a 40  $\mu\text{m}$  thick plastic target rippled on the surface with  $\lambda = 30 \mu\text{m}$  wavelength and 2.5  $\mu\text{m}$  amplitude. For the radiation transport in the hydro simulation, non-LTE opacity model (Klapisch *et al.* 1998) was used. The x-ray heating resulted in a  $\sim 3$ -fold decrease of density at the

ablation front, which, according to (12) resulted in increasing the ablative velocity to  $3 \times 10^5$  cm/s.

The initial amplitude of the ripples is the same, but their growth is seen to be more pronounced in the right, pure CH half of the target. The experiment demonstrates, and simulations reproduce lower amplitude and higher frequency of the oscillations in the coated part of the target. According to the theory, the ablation front ripple amplitude in this part does not grow at all; the small observed growth of  $\delta m$  is fully due to the flattening of the rippled shock front. With a higher oscillation frequency, the theory predicts the phase reversal of  $\delta m$  to occur at about 1.5 ns, much earlier than that observed in Fig. 6(b). Due to lower oscillation amplitude, the experiment did not resolve this phase reversal, but the simulations confirm that it happens between 1.5 and 2.5 ns.

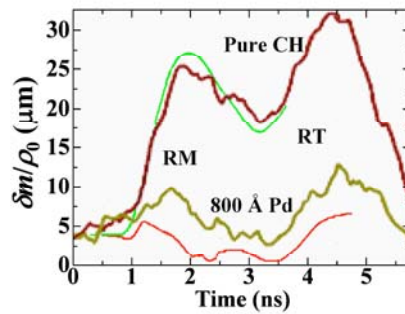


**Figure 6.** Observed (thick lines) and simulated (thin lines) amplitude of the dominant Fourier mode vs. time for the uncoated and coated parts of the plastic target.

Similar experiments with 40  $\mu\text{m}$  thick plastic targets rippled at  $\lambda = 20$  and 30  $\mu\text{m}$  have been later made on the OMEGA laser (Gotchev *et al.* 2006), with Kirkpatrick-Baez microscope used as an imager for face-on x-ray radiography. These experiments have been made at irradiation intensity of 420 TW/cm<sup>2</sup>, much higher than in (Aglitskiy 2001a, 2002), which made it possible to detect the phase reversal of  $\delta m$  within 1 ns. Results of these accurate measurements turned out to be incompatible with modeling of laser-target interaction incorporating flux-limited Spitzer thermal conductivity: No choice of the flux limiter value  $f$  could make the simulations match both the 1D measurements of shock breakout time and the 2D observations of the  $\delta m$  evolution. The matching had only been achieved with the aid of nonlocal model of electron thermal transport (Goncharov *et al.* 2006). The data obtained from observations of the ablative RM oscillations therefore provided the first indication of the nonlocal character of heat transport in laser-driven targets.

## 4. Feedout

Consider a planar shock wave breaking out at the rippled rear surface of a target, behind which there is no low-density material, only vacuum, or a low-density gas whose presence does not affect the hydrodynamics of the shocked heavy fluid. This corresponds to the limiting case  $A = -1$  of heavy-to-light classical RM instability. Such shock-free-surface interaction does not produce any material interface or transmitted shock wave. Only a rarefaction wave reflected back into the shocked target material is produced. This



particular case of a strong rarefaction wave that decompresses to zero pressure is sometimes referred to as an expansion wave.

When a planar or spherical shock wave arrives from the irradiated front or outer surface of a target to its rippled rear or inner surface, the shocked target is turned into a gas/plasma (no material strength remains), and a rippled rarefaction wave is reflected into the shock-compressed target. It brings perturbations to the ablation front, thereby feeding the seeds of the subsequent RT growth (cf. Fig. 3, right). This mechanism of RT seeding by a rippled rarefaction or expansion wave is called feedout. It had been studied in detail in planar geometry (Betti *et al.* 1998b, Smitherman *et al.* 1999, Shigemori *et al.* 2000, Velikovich *et al.* 2001, Aglitskiy *et al.* 2001b, 2002). Here is how the feedout proceeds.

The shock wave breaking out at the rear surface of the ICF target is typically strong enough for complete vaporization of the shocked material after its decompression. The shocked material therefore expands as a gas, forming a centered rarefaction/expansion wave (see Zel'dovich & Raizer 2002, pp. 33-43, 766-770). The head of the expansion wave propagates back into the shock-compressed material with local speed of sound  $c_s$ , whose value is uniform in the shocked target volume because the non-uniformity is localized at its rear surface. Its tail expands at the constant velocity  $v_{\text{exp}} = 2c_s/(\gamma - 1)$  in the opposite direction, into the vacuum, representing the expansion front, where the density and speed of sound vanish.

When the planar shock wave arrives to the rippled rear surface of the target, it first reaches the valleys, and later the peaks of the ripples. The time delay between these two instants is  $2\delta x_0/D$ , where  $2\delta x_0$  is the initial peak-to-valley ripple amplitude, and  $D$  is the shock velocity. The expansion starts from the valleys, while the shock wave continues propagating through the dense target material before reaching the peaks. Therefore the leading edge of the rippled reflected rarefaction wave always has the same phase as the initial surface ripple. The leading edge first reaches the planar front surface of the target where it was initially thinner, triggering the RT growth in phase with the initial distribution of the areal mass non-uniformity  $\delta m$ : the initially thin and thick parts of the target grow thinner and thicker, developing into the bubbles and spikes, respectively, at the ablation front, as predicted by Betti *et al.* 1998b. Such development had indeed been observed in face-on radiographic measurements in experiments on Gekko-XII laser with 25  $\mu\text{m}$  thick plastic targets rippled at the rear surface with  $\lambda = 100 \mu\text{m}$  (Shigemori *et al.* 2000).

On the other hand, the velocity of free expansion of the shocked plasma into vacuum typically exceeds the velocity  $D$  of the shock front propagating in the same direction. Therefore while the shock front propagates to the peaks, the expansion front originated from the valleys is ahead of it. The fully formed expansion front thus reverses its phase with respect to the initial surface ripples, peaks and valleys changing places. Indeed, such phase reversal of the expansion front had been observed with side-on x-ray radiography by Shigemori *et al.* 2000.

If the target thickness is not small compared to the ripple wavelength, then the rippled rarefaction wave itself affects the distribution of the areal mass in the target. When the shock front breaks out at the valley, the decompression starts from there, while the high pressure is still maintained in the shock wave propagating to the peaks. The

resulting lateral pressure gradient starts driving the mass from the peaks to the valleys, decreasing the pressure at the peak locations and increasing it near the valley. The mass flow continues, overshooting the pressure equilibrium situation and building up a reversed pressure gradient (Velikovich *et al.* 2001). These sonic oscillations of the areal mass continue until the leading edge of the expansion wave breaks out at the ablation front, triggering the RT growth. The key difference between such oscillations in shock and rarefaction waves is that the restoring force is weaker in the rarefaction wave, hence the amplitude of the areal mass oscillations is much larger. For ideal gas EOS, these oscillations are described by explicit analytical formulas (Velikovich *et al.* 2001, 2005). At late time and for gas  $\gamma$  not too close to unity but less than 2, these oscillations are well described by the asymptotic formula

$$\frac{\delta m}{\delta m_0} = \frac{4\sqrt{2}[\gamma - 1 + \sqrt{2\gamma(\gamma - 1)}]}{(\gamma - 1)^2 \Omega t} \sin \Omega t, \quad (9)$$

where

$$\Omega = \left[ \frac{2(\gamma - 1)}{\gamma + 1} \right]^{(\gamma - 1)/(3 - \gamma)} kc_s.$$

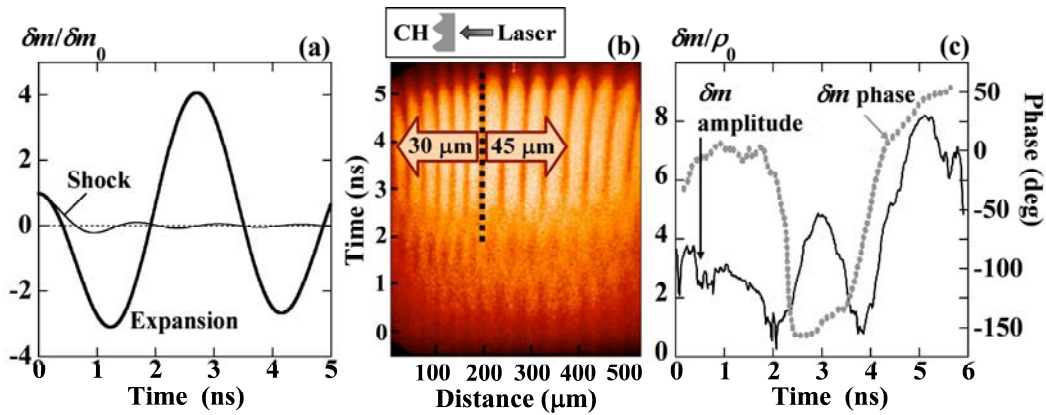


Figure 7. (a) Time histories of the normalized areal mass modulation amplitude in a rippled expansion and shock waves for shock velocity  $D = 4 \times 10^6$  cm/s, ripple wavelength  $\lambda = 30 \mu\text{m}$ , all other parameters being the same as in Fig. 3.3. The origin  $t = 0$  corresponds to the start of the laser pulse for the rippled shock wave and to the moment of shock breakout at the rear surface of the target for the rippled expansion wave. (b) Streak record of a target rippled on the rear side with two wavelengths: 30  $\mu\text{m}$  and 45  $\mu\text{m}$ . (c) Amplitude (black) and phase (gray) of the dominant Fourier mode vs. time for the 45  $\mu\text{m}$  wavelength. The inset shows schematic of the experiment.

They are illustrated here by Fig. 7(a) plotted for  $\gamma = 5/3$  and the same shock velocity  $D = 4 \times 10^6$  cm/s as in the example of Fig. 5. For comparison, oscillations of the shock front transmitted into the target in the conditions of Fig. 5 are shown on the same figure. The rarefaction and shock contributions to  $\delta m$  have been normalized differently here, to facilitate the comparison. For the rippled expansion wave  $\delta m_0 = \rho_0 \delta x_0$ , where  $\delta x_0$  is the initial amplitude of the rear surface ripple; for the shock wave

$\delta m_0 = (\rho_a - \rho_0)\delta x_0$ , where  $\delta x_0$  is the initial amplitude of the front surface ripple. The shock front ripple is seen to flatten out once the shock propagates one ripple wavelength. The rippled expansion wave of Fig. 7(a) reverses the phase of  $\delta m$  when its leading propagates a quarter of the ripple wavelength. Later, when the leading edge propagates two-thirds of the ripple wavelength, the areal mass modulation reaches its first negative peak, about 3 times its initial amplitude with inverted phase.

For these large oscillations of  $\delta m$  to be observable, the ratio of target thickness  $L$  to the ripple wavelength  $\lambda$  should be large enough:  $L/\lambda > 0.9$  to observe the first phase reversal,  $L/\lambda > 2.7$  to observe the first peak of  $\delta m$  with inverted phase (Aglitskiy *et al.* 2002). For the targets used by Shigemori *et al.* 2000,  $L/\lambda = 0.25$ , which means that their targets were too thin to see the dip in  $\delta m$ . The phase reversal of  $\delta m$  in a rippled expansion wave was first observed in the experiments with 85  $\mu\text{m}$  thick Al targets rippled on the rear side at  $\lambda = 50 \mu\text{m}$  and driven by the Nova hohlraum (Smitherman *et al.* 1999). When the head of the rippled expansion wave breaks out at the ablation front, it starts the target acceleration and triggers the RT growth of in the  $\delta m$  in the positive direction, as explained above. If  $\delta m$  has already changed phase in the rippled rarefaction wave due to the lateral mass flow in the volume of the target, but has not yet reached its maximum with inverted phase at the onset of acceleration, then it must change the direction of growth, and eventually change phase again due to the areal mass redistribution at the ablation front. Such behavior had been seen in the simulations of Smitherman *et al.* 1999 but not resolved experimentally.

The first direct observation of the feedout in the regime  $L/\lambda > 1$  where the areal mass redistribution in the rippled expansion wave is important have been reported by Aglitskiy *et al.* 2001b, 2002. We observed the whole evolution of perturbations caused by feedout in a planar target: large-amplitude areal mass oscillation in a rippled expansion wave, two phase reversals and a subsequent RT growth. Figure 7(b) shows the streak record obtained for a 60  $\mu\text{m}$  thick plastic target rippled on the rear side at  $\lambda = 30 \mu\text{m}$  and 45  $\mu\text{m}$  for its left and right half, respectively. The light and dark stripes indicating, respectively, low and high areal mass, are seen at early time and then they disappear. Later the stripes reappear, but the light and dark ones change places, indicating a phase reversal, similar to that shown in figure 5(b). Shortly after this, the RT growth of  $\delta m$  in the positive direction begins, and the phase of  $\delta m$  is reversed again. Figure 7(c) shows the time histories of the peak-to-valley amplitude and phase of the dominant Fourier mode, normalized as above, for the left, short-wavelength half of the target. The two phase reversals of  $\delta m$  are clearly observed.

## 5. Shock deceleration of an ablation front

All the experiments discussed in Section 3 refer to the “light-to-heavy” case of the ablative RM instability, when the shock wave originates at the ablation front and propagates from it into the dense target plasma. According to the theory (Goncharov 1999, Goncharov *et al.* 2006), stability of a non-accelerated ablation front is an intrinsic property. Therefore the theory predicts that the ablation front should remain stable even when the shock wave arrives from the dense target plasma (the “heavy-to-light” case). Similarly to the feedout, the process we are interested in starts when a shock wave breaks out at the plasma boundary. In this case, however, the boundary represents the ablation

front, where a constant pressure is maintained by the laser, rather than the free rear surface at zero pressure.

Our experiments were made with targets consisting of planar plastic foils rippled on the rear side (single-mode ripple wavelength  $\lambda = 45 \mu\text{m}$ , peak-to-valley amplitude  $2\delta x_0 = 2 \mu\text{m}$ ) and a planar layer of divinyl benzene foam (10-20% of solid CH density) separated from the CH foil by a vacuum gap, see Fig. 2(a). The front side of the plastic foil is irradiated by a 4 ns Nike pulse with peak intensity about  $50 \text{ TW/cm}^2$ . Laser radiation accelerates the CH foil across a vacuum gap until it collides with a lower-density foam layer. While the target is accelerated, a fast Rayleigh-Taylor (RT) growth of the single-mode perturbation at the ablation front is observed. After the collision, the velocity of the ablation front is seen to remain constant, and the RT growth is quenched.

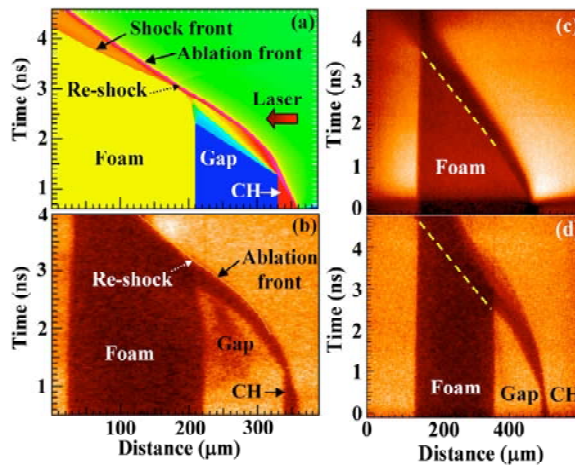


**Figure 8.** (a) Simulated density map and (b) side-on x-ray streak record (b) for a CH foil collision with a foam layer. (c) Side-on x-ray streak record for a directly irradiated 10% solid density foam layer. (d) Same for a CH foil colliding with such a layer.

Figures 8(a), (b) demonstrate the simulated and observed 1D time history of a collision for a target with a  $30 \mu\text{m}$  thick CH foil separated by a  $120 \mu\text{m}$  gap from a  $200 \mu\text{m}$  thick, 10% solid CH density foam layer. Figure 8(a) is a simulated density map on the  $(x, t)$  plane. The laser irradiation drives a strong shock wave into the CH foil, compresses it and sets it into the motion at constant mass velocity that is associated with the shock wave. Before the start of its acceleration, the trajectory of the ablation front on the  $(x, t)$  plane is straight. The compressed CH foil plasma starts to accelerate following the break-out of this shock at its rear surface, when the rarefaction wave reflected from it reaches the ablation front ( $t \approx 1.4 \text{ ns}$ ). The acceleration makes the trajectory of the ablation front on the  $(x, t)$  plane convex. Then at  $t \approx 3 \text{ ns}$  the foil accelerated to  $\sim 10^7 \text{ cm/s}$  collides with the foam layer. Simulations indicate that the collision briefly produces a pressure of  $\sim 30 \text{ Mbar}$ , which is 3.5 times greater than the pressure  $\sim 8 \text{ Mbar}$  maintained by the laser at the ablation front. This pressure pulse generates two strong shock waves. One of them propagates forward into the thick foam layer, while the other propagates back into the thin, compressed and partly ablated CH foil plasma. The ablation front is re-shocked from the dense plasma side. The ablation front rapidly decompresses from the high shock pressure to  $\sim 8 \text{ Mbar}$ . The rarefaction wave that emerges from the ablation

front at the instant of its re-shock carries the reduced pressure back to the shock wave propagating into the foam, rapidly slowing it down.

This shock is then fully determined by the ablative pressure maintained by the laser ablation and the foam density, as evidenced by the shape of this shock's  $(x, t)$  trajectory on Fig. 8(a), which is concave for a short time interval, and then a straight line after  $t \approx 3.2$  ns. The re-shock impulsively changes the velocity of the ablation front, which then stays constant, and its  $(x, t)$  trajectory becomes straight again starting from  $t \approx 3.1$  ns. Figure 8(c), (d) compare velocities of the shocks in 10% solid density foam produced by direct irradiation of the foam with Nike beams (a) and by collision of the laser-accelerated CH foil with the foam layer (b). The slope of the dashed lines exactly corresponds to the shock velocity in the latter case, averaged from the instant of collision to the observed shock breakout at the rear surface, and it is very close to the observed velocity of the shock wave driven into the foam directly by the laser. The constant velocities of the shock front in the foam and of the ablation fronts at this stage are fully determined by the ablative pressure maintained by the laser and the foam density.

Observed and simulated evolution of the dominant Fourier mode of the areal mass modulation is shown in Fig 9(a). The thick lines with approximate error bars present the experimental data from the face-on images. The pink line corresponds to the same conditions as Fig. 8(a), (b), the light blue line to a higher foam density: 10% and 20% of solid, respectively. The signal is normalized with respect to its initial value  $\delta m_0 = \rho_0 \delta x_0$ . The small time shift between these two curves prior to the collision is due to a combination of difference in the actual foil thickness and the timing relative to the start of the laser pulse. Thin red and blue lines show the simulation results obtained in two-dimensional simulations for the same conditions as pink and light blue lines, respectively, with plasma radiation taken into account.

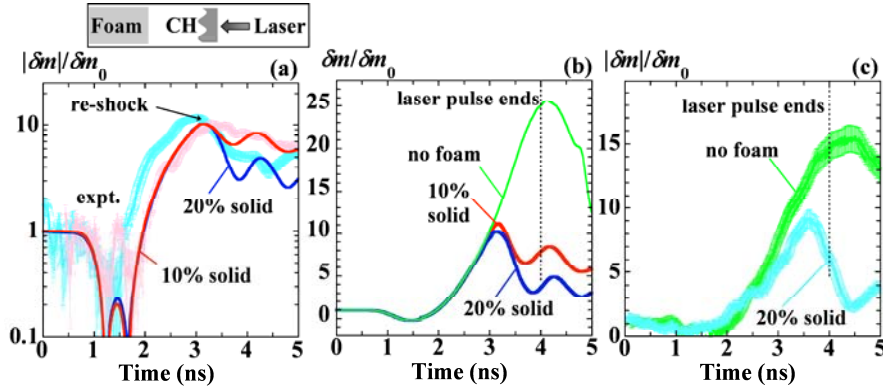


**Figure 9.** (a) Observed (thick, with approximate error bars) and simulated (thin lines) time history of  $\delta m$  in the target. Arrow indicates the instant of re-shock on simulated lines. (b) Simulated time history of the  $\delta m$  in a CH foil freely accelerated (green line) and colliding with a foam layer (red and blue lines). (c) Observed time history of  $\delta m$  in the CH foil rippled on the rear side (green line with approximate error bars) and in such foil colliding with a foam layer (light blue line).

Figure 9(a) shows that the early-time minimum and two phase reversals characteristic of the feedout. They are not well-resolved here because our CH foil is thinner than those used in the feedout experiments, see Section 4. Our observations are

nevertheless consistent with the presence of this minimum and with the corresponding delay in the onset of the RT growth. It is thereby seeded by the feedout mechanism, see Section 4.

The RT growth is quenched when the collision occurs and the ablation front is re-shocked. A re-shock of a material interface would (re)start a classical RM growth of its perturbations. Since the linear RM growth rate is proportional to the initial ripple amplitude, a “heavy-to-light” re-shock of a material interface after a substantial RT or RM amplification of its non-uniformities would give rise to a rapid growth of the areal mass modulation amplitude in the negative direction, implying a quick reversal of its phase. A similar increase of the RM growth rate at a re-shocked interface has been observed in shock-tube experiments (Leinov *et al.* 2008). Our results presented in Fig. 9(a) do not demonstrate such a behavior. Instead, the growth of the areal mass modulation amplitude is seen to end with the re-shock and to be followed by decaying oscillations around a nonzero average value. This effect is robust and caused entirely by the collision.

As demonstrated in Figs. 9(b), (c), the quenching is not due to nonlinear saturation or any other mechanism that would slow down the RT growth in the absence of the collision. Without the collision, the simulated RT growth (green line in Fig. 9(b)) would continue until the target burns through, or is broken up by the instability, or the laser pulse ends. The same is observed in the experiment, Fig. 9(c). Here the collision occurs at 3.5 ns, later than in Figs. 9(a), (b), due to lower laser intensity and wider gap between the foil and the foam, but still well within the 4 ns Nike pulse.

Decaying oscillations of a non-accelerated ablation front seen in Figs. 9(a), (b) are not the low-frequency ablative RM oscillations (cf. Figs. 4, 5). These are oscillations around a non-zero average. The ablation front ripples, which provide the largest contribution to the observed areal mass modulation amplitude  $\delta m$ , do not change phase. On the other hand, the simulated and observed oscillation period,  $\sim 1$  ns, is close to the sound wave period  $\lambda/c_s$ , where  $\lambda = 45 \mu\text{m}$ , and the speed of sound  $c_s$  in the re-shocked foil plasma is estimated from the simulations to be  $\sim 5 \times 10^6 \text{ cm/s}$ . The observed time history of  $\delta m$  therefore involves fast areal mass oscillations in the rippled rarefaction wave that emerges from the ablation front after the re-shock (as in the case of feedout, cf. Fig. 7(a)), superimposed upon the slow, also oscillatory, evolution due to the ablative RM instability. Indeed, all our simulation results show that the changes in  $\delta m$  after the collision accumulate in the volume of the plasma reached by the rarefaction wave.

Therefore, our observations prove that the ablation front becomes stable as soon as its acceleration stops, in agreement with the theory.

## 6. Impulsive Loading

The process called impulsive loading can be idealized as a fast release of a finite energy in a thin layer near the surface  $x = 0$  of a half-space  $x \leq 0$  filled with a uniform material at rest. Impulsive loading had been studied since the 1950s (Häfele 1955, Zel’dovich & Raizer 2002 pp. 820-849 and references therein), when it was visualized as an explosion of a thin surface layer of explosive, or a concentrated impact of a thin, light plate carrying a finite kinetic energy. A short laser pulse depositing a finite thermal energy in a thin surface layer of a target before being turned off also can act as an

impulsive load. Impulsive loading sends a strong shock wave into the target, which is immediately followed by an expansion wave that gradually decelerates it. In a sense, the impulsive loading is similar to a planar blast wave (Sedov 1959), and it also produces a self-similar flow of the shocked material. The difference is that the impulsive loading involves free expansion of this material to zero pressure (in a blast wave, the minimum pressure in a rarefaction wave following the shock wave is finite), which implies a different kind of self-similarity, see the discussion by Zel'dovich & Raizer 2002, Chapter XII.

Renewed interest to the impulsive loading in the area of direct-drive laser fusion emerged several years ago. It is due to the recent proposals of using a short laser pulse called a spike or a picket prior to the main drive pulse in order to make the target more resistant to laser imprint (Metzler *et al.* 2002, 2003) and to shape the target adiabat (Goncharov *et al.* 2003, Anderson & Betti 2003, Betti *et al.* 2005). The stabilizing effects of the impulsive loading are caused by the density profile in the expansion wave that follows the decaying shock wave. Since the density increases into the target, the shock wave driven by the main pulse slows down as it propagates, and so does the ablation front pushing it. Deceleration stabilizes the ablation front much more strongly than the “rocket effect” responsible for the ablative RM oscillations, which results in effective mitigation of perturbation growth due to the non-uniformities of both laser irradiation and target surface (Metzler *et al.* 1999). Moreover, as the shock wave driven by the main pulse slows down, the density of the shocked target material increases and its temperature decreases. We end up with a “tailored adiabat” of the target, where adiabat is defined as  $\alpha = p / p_F \propto \rho^{-5/3}$ ,  $p$  and  $p_F$  being, respectively, the pressure in the target and the pressure of degenerate electron Fermi-gas at the given density  $\rho$ . Lower density in the outer layers of the target ensures a higher ablation velocity  $v_a$ , hence, lower rate of the RT growth, cf. Eq. (3), and thereby better stability of implosion. On the other hand, high adiabat  $\alpha$  of the fuel makes it difficult to compress. The kinetic energy of the target requires for its ignition scales as a power of the in-flight adiabat  $\alpha_{if}$ :  $E_{ig} \propto \alpha_{if}^k$ , where the high power  $k$  is estimated to be between 1.8 (Herrmann *et al.* 2001, Kemp *et al.* 2001) to 2.4 (Betti *et al.* 2002). Using the impulsive loading to tailor the target adiabat, we can achieve stable implosion and high compression of the fuel simultaneously.

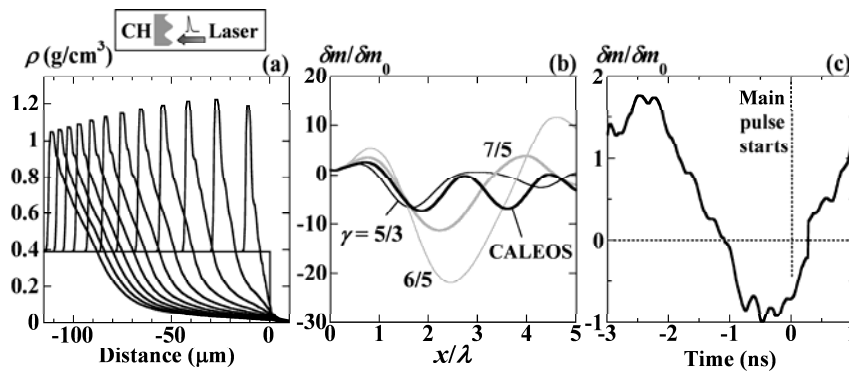


**Figure 10.** (a) Time evolution of a density profile in a foam layer irradiated by a 0.325 ns long pulse. The profiles are shown with a 1 ns time interval. (b) Simulated amplitudes of the dominant Fourier mode vs. normalized shock travel distance for an impulsively loaded rippled target. (c)

Observed dominant Fourier mode vs. time for a rippled plastic target loaded with a 0.3 ns long pulse. The inset shows schematic of the experiment.

Figure 10(a) illustrates the 1D flow produced by the impulsive loading in a planar geometry. It shows a sequence of simulated density profiles resulting from the irradiation of a CH foam layer (density  $0.39 \text{ g/cm}^3$ ) with a 0.325 ns long KrF pulse at  $4.1 \text{ TW/cm}^2$ . A graded density profile produced by the shock-expansion flow expands with time in approximately self-similar way. After being shocked, each particle first moves in the direction of shock propagation. Later, the negative pressure gradient slows it down and accelerates it in the opposite direction.

Both rippled shock and expansion waves tend to oscillate as they propagate at constant velocity into an unperturbed fluid. Oscillations of the expansion wave are stronger, cf. Fig. 7(a). Evolution of perturbations in the shock-expansion flow generated by impulsive loading was first studied theoretically by Velikovich *et al.* 2003. It was found that the coupled shock and expansion waves produce much stronger oscillations than either a shock wave or an expansion wave separately. This happens because the shock wave decelerates, weakening the restoring force that acts upon the shock ripples. As the decelerating shock wave propagates through the target, its modulation amplitude grows, exceeding the initial amplitude by a factor of 2 or more. The oscillating areal mass modulation amplitude  $\delta m$  reaches the peak values that exceed its initial value  $\delta m_0 = \rho_0 \delta x_0$  by a factor of 5-7 or more and reverses its phase several times after the laser pulse is over.

This behavior is illustrated by Fig. 10(b). Here the areal mass modulation amplitude is shown vs. the normalized distance traveled by the shock wave,  $x/\lambda$ , for ideal-gas equations of state with  $\gamma$  varied from  $6/5$  to  $5/3$  and CALEOS model equation of state of plastic foam. The oscillations are seen to be the strongest for the most compressible EOS,  $\gamma = 6/5$ , which reveals the physical similarity of this strong effect with Vishniac's instability of a blast wave (Vishniac 1983, Ryu & Vishniac 1987). As explained by Velikovich *et al.* 2005, the Vishniac's instability is also driven by the instability of a planar expansion wave at low  $\gamma$ .

Figure 10(c) shows the first experimental observation of such oscillations reported by Weaver *et al.* 2004. A 0.3 ns long,  $7.7 \text{ TW/cm}^2$  KrF laser spike irradiated the target 3 ns prior to the arrival of the main pulse at  $t = 0$ , rapidly depositing  $2.3 \text{ kJ/cm}^2$  of energy into a  $40 \text{ }\mu\text{m}$  thick plastic foil rippled on the front surface with  $\lambda = 30 \text{ }\mu\text{m}$ ,  $\delta x_0 = 2.5 \text{ }\mu\text{m}$ . About  $t = 0$  the shock wave driven by the spike breaks out at the rear surface of the target, which corresponds to  $kx_s = 8.37$  in Fig. 10(a). Between  $t = -2.7 \text{ ns}$  and  $t = 0$  the laser is off, and the evolution of  $\delta m$  seen in Fig. 10(c) are represents free oscillations of the shock-expansion flow described above. We see the expected strong oscillations of the areal mass and its phase reversal at about the same time as predicted.

Detailed experimental study of the strong shock wave and areal mass oscillations associated with impulsive loading of planar targets is still ahead. It will provide valuable data for benchmarking hydro codes and testing the EOS approximations in the Mbar pressure range. The observable oscillations take place when the laser is off and are fully determined by the integral characteristics of the short pulse: the energy deposited near the target surface and the preheat of the target material by x-rays or fast electrons, if any.



Therefore, study of these oscillations can be largely separated from the complicated physics of laser-plasma interaction.

## 7. Conclusions

A considerable progress had been made in the last decade in observation and understanding the RM-type hydrodynamics processes. An extensive data base has been accumulated for benchmarking hydrocodes and testing theoretical models. Agreement between the experimental data and simulation result in most cases is reasonably good, which indicates that the basic physics underlying the RM-type phenomena is understood correctly. A decisive role in this progress has been played by the monochromatic x-ray imaging, which proved to be a powerful tool for observing dynamics of ICF targets and probing the lateral mass redistribution due to hydro instabilities, waves and other transient processes.

Of course, much more needs to be done to fine-tune the details and to make sure that all the relevant physics, such as equation of state and radiation transfer/preheat, is properly accounted for. Some of the theoretically predicted RM-type processes are yet to be observed, for example, the instability on the material interface that is dynamically formed at collision of two planar foils, when at least one of the colliding foils is rippled (Velikovich *et al.* 2000). In addition to the existing ICF laser facilities, the new 10-kJ class lasers, such as LIL, Shenguang-III and Luch, open the opportunities for such experiments to be carried out in France, China and Russia. This research will be an important contribution to the efforts aimed at achieving ignition, fusion energy gain, and eventually, fusion energy production, on NIF in the U. S., LMJ in France and next-generation laser facilities of the future.

*Acknowledgments.* We are grateful to Dr. S. I. Abarzhi for her suggestion to present this review at the international conference “Turbulent mixing and beyond” and to participants of this conference for valuable discussion. We thank Nike Laser Crew for their excellent technical support and Dr. R. H. Lehmberg for helpful discussion. This work was supported by the U. S. Department of Energy, Defense Programs.

## References

- Aglitskiy, Y., Lehecka, T., Deniz, A., Hardgrove, J., Seely, J., Brown, C., Feldman, U., Pawley, C., Gerber, K., Bodner, S., Obenschain, S., Lehmberg, R., McLean, E., Pronko, M., Sethian, J., Schmitt, A., Sullivan, C., Holland, G. & Laming, M. 1996 X-ray emission from plasmas created by smoothed KrF laser irradiation. *Phys. Plasmas* **3**, 3438-3447.
- Aglitskiy, Y., Velikovich, A. L., Karasik, M., Serlin, V., Pawley, C. J., Schmitt, A. J., Obenschain, S. P., Mostovych, A. N., Gardner, J. H. & Metzler, N. 2001a Direct observation of mass oscillations due to ablative Richtmyer-Meshkov instability in plastic targets. *Phys. Rev. Lett.* **87**, 265001.
- Aglitskiy, Y., Velikovich, A. L., Karasik, M., Serlin, V., Pawley, C. J., Schmitt, A. J., Obenschain, S. P., Mostovych, A. N., Gardner, J. H. & Metzler, N. 2001b Direct observation of feedout-related mass oscillations in plastic targets. *Phys. Rev. Lett.* **87**, 265002.

- Aglitskiy, Y., Velikovich, A. L., Karasik, M., Serlin, V., Pawley, C. J., Schmitt, A. J., Obenschain, S. P., Mostovych, A. N., Gardner, J. H. & Metzler, N. 2002 Direct observation of oscillations due to ablative Richtmyer-Meshkov instability and feedout in planar plastic targets. *Phys. Plasmas* **9**, 2264-2276.
- Aglitskiy, Y. Metzler, N., Karasik, M., Serlin, V., Velikovich, A. L., Obenschain, S. P., Mostovych, A. N., Schmitt, A. J., Weaver, J., Gardner, J. H. & Walsh, T. 2006 Perturbation evolution started by Richtmyer-Meshkov instability in planar laser targets. *Phys. Plasmas* **13**, 080703.
- Anderson, K. & Betti, R. 2003 Theory of laser-induced adiabat shaping in inertial fusion implosions: The decaying shock. *Phys. Plasmas* **10**, 4448-4462.
- Atzeni, S. & Meyer-ter-Vehn, J. 2004 *The Physics of Inertial Fusion: Beam Plasma Interaction, Hydrodynamics, Hot Dense Matter*. Oxford University Press.
- Besnard, D. 2007 The megajoule laser program - ignition at hand. *Eur. Phys. J. D* **44**, 207-213.
- Betti, R., Goncharov, V. N., McCrory, R. L. & Verdon, C. P. 1998a Growth rates of the ablative Rayleigh-Taylor instability in inertial confinement fusion. *Phys. Plasmas* **5**, 1446-1454.
- Betti, R., Lobatchev, V. & McCrory, R. L. 1998b Feedout and Rayleigh-Taylor seeding induced by long wavelength perturbations in accelerated planar foils. *Phys. Rev. Lett.* **81**, 5560-5563.
- Betti, R., Anderson, K. & Goncharov, V. N. 2002 Deceleration phase of inertial confinement fusion implosions. *Phys. Plasmas* **9**, 2277-2286.
- Betti, R., Anderson, K., Knauer, J., Collins, T. J. B., McCrory, R. L., McKenty, P. W. & Skupsky, S. 2005 Theory of laser-induced adiabat shaping in inertial fusion, implosions: The relaxation method. *Phys. Plasmas* **12**, 042703.
- Betti, R., Zhou C. D., Anderson, K. S., Perkins L. J., Theobald, W. & Solodov A. A. 2007 Shock ignition of thermonuclear fuel with high areal density. *Phys. Rev. Lett.* **98**, 155001.
- Boehly, T. R., Craxton, R. S., Hinterman, T. H., Kelly, J. H., Kessler, Kumpan, S. A., Letzring, S. A., McCrory, R. L., Morse, S. W. B., Seka, W., Skupsky, S., Soures, J. M. & Verdon, C. P. 1995 The upgrade to the OMEGA-laser-system. *Rev. Sci. Instrum.* **66**, 508-510.
- Bodner, S. E. 1974 Rayleigh-Taylor instability and laser-pellet fusion. *Phys. Rev. Lett.* **33**, 761-764.
- Bodner, S. E., Colombant, D. G., Gardner, J. H., Lehmberg, R. H., Obenschain, S. P., Phillips, L., Schmitt, A. J., Sethian, J. D., McCrory, R. L., Seka, W., Verdon, C. P., Knauer, J. P., Afeyan, B. B. & Powell, H. T. 1998 Direct-drive laser fusion: Status and prospects. *Phys. Plasmas* **5**, 1901-1918.
- Brown, C., Seely, J., Feldman, U., Obenschain, S., Bodner, S., Pawley, C., Gerber, K., Serlin, V., Sethian, J., Aglitskiy, Y., Lehecka, T. & Holland, G. 1997a X-ray imaging of targets irradiated by the Nike KrF laser. *Rev. Sci. Instrum.* **68**, 1099-1102.
- Brown, C., Seely, J., Feldman, U., Obenschain, S., Bodner, S., Pawley, C., Gerber, K., Sethian, J., Mostovych, A., Aglitskiy, Y., Lehecka, T. & Holland, G. 1997b High resolution x-ray imaging of planar foils irradiated by the Nike KrF laser. *Phys. Plasmas* **4**, 1397-1401.

- Cabot W. H. & Cook, A. W. 2006 Reynolds number effects on Rayleigh-Taylor instability with possible implications for type-Ia supernovae. *Nature Physics* **2**, 562-568.
- Chapman, P. R. & Jacobs, J. W. 2006 Experiments on the three-dimensional incompressible Richtmyer-Meshkov instability. *Phys. Fluids* **19**, 074101.
- Chou, P. C., Corleone, J. & Carp, R. R. 1976 Criteria for jet formation from impinging shells and plates. *J. Appl. Phys.* **47**, 2975.
- Deniz, A., Lehecka, T., Lehmberg, R. H. and Obenschain, S. P. 1998 Comparison between measured and calculated nonuniformities of Nike laser beams smoothed by induced spatial incoherence. *Opt. Commun.* **147**, 402-410.
- Dimonte, G. & Remington, B. 1993 Richtmyer-Meshkov experiments on the Nova laser at high compression. *Phys. Rev. Lett.* **70**, 1806-1809.
- Dimonte, G., Frerking, C. E., Schneider, M. & Remington, B. 1996 Richtmyer-Meshkov instability with strong radiatively driven shocks. *Phys. Plasmas* **3**, 613-630.
- Dimonte G., Ramaprabhu, P. & Andrews, M. 2007 Rayleigh-Taylor instability with complex acceleration history. *Phys. Rev. E* **76**, 046313.
- Eichelberger, R. J. & Pugh, E. M. 1952 Experimental verification of the theory of jet formation by charges with lined conical cavities. *J. Appl. Phys.* **23**, 537-542.
- Endo, T., Shigemori, K., Azechi, H., Nishiguchi, A., Mima, K., Sato, M., Nakai, M., Miyanaga, N., Matsuoka, S., Ando, A., Tanaka, K. A. & Nakai, S. 1995 Dynamic behavior of rippled shock waves and subsequently induces areal-density perturbation growth in laser-irradiated foils. *Phys. Rev. Lett.* **74**, 3608-3611.
- Eyharts, P., Di-Nicola, J. M., Feral, C., Germain, E., Graillet, H., Jequier, F., Journot, E., Julien, X., Luttmann, M., Lutz, O. & Thiell, G. 2006 The LIL facility: An experimental tool for laser-matter interaction. *J. Phys. IV* **133**, 727-730.
- Erez, L., Sadot, O., Oron, D., Erez, G., Levin, L. A., Shvarts, D. & Ben-Dor, G. 2000 Study of the membrane effect on turbulent mixing measurements in shock tubes. *Shock Waves* **10**, 241-251.
- Garanin, S. G., Zaretskii, A. I., Il'kaev, R. I., Kirillov, G. A., Kochemasov, G. G., Kurunov, R. F., Murugov, V. M. & Sukharev, S. A. 2005 Channel of a high-power laser fusion Luch facility emitting 3.3-kJ, and 4-ns pulses. *Quantum Electron.* **35**, 299-301.
- Glendinning, S. G., Bolstad, J., Braun, D. G., Edwards, M. J., Hsing, W. W., Lasinski, B. F., Louis, H., Miles, A., Moreno, J., Peyser, T. A., Remington, B. A., Robey, H. F., Turano, E. J., Verdon, C. P. & Zhou, Y. 2003 Effect of shock proximity on Richtmyer-Meshkov growth. *Phys. Plasmas* **10**, 1931-1936.
- Goncharov, V. N., Betti, R., McCrory, R. L., Sorotokin, P. & Verdon, C. P. 1996 Self-consistent stability analysis of ablation fronts with Large Froude numbers. *Phys. Plasmas* **3**, 1402-1414.
- Goncharov, V. N. 1999 Theory of the ablative Richtmyer-Meshkov instability. *Phys. Rev. Lett.* **82**, 2091-2094.
- Goncharov, V. N., Knauer, J. P., McKenty, P. W., Radha, P. B., Sangster, T. C., Skupsky, S., Betti, R., McCrory, R. L. & Meyerhofer D. D. 2003 Improved performance of direct-drive inertial confinement fusion target designs with adiabat shaping using an intensity picket. *Phys. Plasmas* **10**, 1906-1918.

- Goncharov, V. N., Gotchev, O. V., Vianello, E., Boehly, T. R., Knauer, J. P., McKenty, P. W., Radha, P. B., Regan, S. P., Sangster, T. C., Skupsky, S., Smalyuk, V. A., Betti, R., McCrory, R. L., Meyerhofer, D. D. & Cherfils-Cl  rouin, C. 2006 Early stage of implosion in inertial confinement fusion: Shock timing and perturbation evolution. *Phys. Plasmas* **13**, 012702.
- Gotchev, O. V. Goncharov, V. N., Knauer, J. P., Boehly, T. R., Collins, T. J. B., Epstein, R., Jaanimagi, P. A. & Meyerhofer, D. D. 2006 Test of thermal transport models through dynamic overpressure stabilization of ablation-front perturbation growth in laser-driven CH foils. *Phys. Rev. Lett.* **96**, 115005.
- H  fele, W. 1955 Zur analytischen behandlung ebener, starker, instation  ren stosswellen. *Z. Naturforsch. A* **10a**, 1006-1016.
- He, X. T. & Zhang, W. Y. 2007 Inertial fusion research in China. *Eur. Phys. J. D* **44**, 227-231.
- Herrmann, M. C., Tabak, M. & Lindl, J. D. 2001 A generalized scaling law for the ignition energy of inertial confinement fusion capsules. *Nucl. Fusion* **41**, 99-111.
- Holder, D. A., Smith, A. V., Barton, C. J. & and Youngs, D. L. 2003 Mix experiments using a two-dimensional convergent shock-tube. *Laser and Particle Beams* **21**, 403-409 (2003).
- Kemp A., Meyer-ter-Vehn J. & Atzeni, S. 2001 Stagnation pressure of imploding shells and ignition energy scaling of inertial confinement fusion targets. *Phys. Rev. Lett.* **86**, 3336-3339.
- Klapisch, M., Bar-Shalom, A., Oreg, J. & Colombant, D. 1998 Non local-thermodynamical-equilibrium effects in the simulation of laser-produced plasmas. *Phys. Plasmas* **5**, 1919-1926.
- Kumar, S., Vorobieff, P., Orlicz, G., Palekar, A., Tomkins, C., Goodenough, C., Marr-Lyon, M., Prestridge, K. P. & and Benjamin, R. F. 2007 Complex flow morphologies in shock-accelerated gaseous flows. *Physica D* **235**, 21-28.
- Lehmberg, R. H. & Rothenberg, J. E. 2000 Comparison of optical beam smoothing techniques for inertial confinement fusion and improvement of smoothin by the use of zero-correlation masks. *J. Appl. Phys.* **87**, 1012-1022.
- Leinov, E., Sadot, O., Formoza, A., Malamud, G., Elbaz, Y., Levin, L. A., Ben-Dor, G., and Shvarts, D. 2008 Investigation of the Richtmyer-Meshkov instability under re-shock conditions. *Phys. Scr.* **T132**, 014014.
- Li, C. P. & Book, D. L. 1991 Instability generated by acceleration due to rarefaction waves. *Phys. Rev. A* **43**, 3153-3156.
- Li, C., Kailasanath, K. & Book, D. L. 1991 Mixing enhancement by expansion waves in supersonic flows of different densities. *Phys. Fluids A* **3**, 1369-1373.
- Lindl, J. D. 1998 *Inertial Confinement Fusion: the Quest for Ignition and Energy Gain Using Indirect Drive*. Springer.
- Manheimer, W. M., Colombant, D. G. & Gardner, J. H. 1982 Steady-state planar ablative flow. *Phys. Fluids* **25**, 1644-1652.
- Mariani, C., Vandenboomgaerde, M., Jourdan, G., Souffland, D. & Houas, L. 2008 Investigation of the Richtmyer-Meshkov instability with stereolithographed interfaces. *Phys. Rev. Lett.* **100**, 2545003.
- Meshkov, E. E. 1969 Instability of the interface between two gases accelerated by a shock wave. *Fluid Dyn.* **4**(5), 101-104.

- Metzler, N., Velikovich, A. L. & Gardner, J. H. 1999 Reduction of early-time perturbation growth in ablatively driven laser targets using tailored density profiles. *Phys. Plasmas* **6**, 3283-3295.
- Metzler, N., Velikovich, A. L., Schmitt A. J. & Gardner, J. H. 2002 Laser imprint reduction with a short shaping laser pulse incident upon a foam-plastic target. *Phys. Plasmas* **9**, 5050-5058.
- Metzler, N., Velikovich, A. L., Schmitt, A. J., Karasik, M., Serlin, V., Mostovych, A. N., Obenschain, S. P., Gardner, J. H. & Aglitskiy, Y. 2003 Laser imprint reduction with a shaping pulse, oscillatory Richtmyer-Meshkov to Rayleigh-Taylor transition and other coherent effects in plastic-foam targets. *Phys. Plasmas* **10**, 1897-1905.
- Motl, J., Niederhaus, J. H. J., Rarjan, D., Oakley, J. G., Anderson, M. H. & Bonazza, R. 2007 Experimental study for ICF-related Richtmyer-Meshkov instabilities. *Fusion Science and Technology*, **52**, 1079-1083.
- Mueschke, N. J., Andrews, M. J., and Schilling, O. 2006 Experimental characterization of initial conditions and spatio-temporal evolution of a small-Atwood-number Rayleigh-Taylor mixing layer. *J. Fluid Mech.* **567**, 27-63 (2006).
- Niederhaus, C. E. and J. W. Jacobs, J. W. 2003 Experimental study of the Richtmyer-Meshkov instability of incompressible fluids. *J. Fluid Mech.* **485**, 243-277.
- Obenschain, S. P., Bodner, S. E, Colombant, D., Gerber, K., Lehmburg, R. H., McLean, E. A., Mostovych, A. N., Pronko, M. S., Pawley, C. J., Schmitt, A. J., Sethian, J. D., Serlin, V., Stamper, J. A., Sullivan, C. A., Dahlburg, J. P., Gardner, J. H., Chan, Y., Deniz, A.V., Hardgrove, J., Lehecka, T. & Klapisch M 1996 The Nike KrF laser facility: Performance and initial target experiments. *Phys. Plasmas* **3**, 2098-2107.
- Obenschain, S. P., Colombant, D. G., Karasik, M., Pawley, C. J., Serlin, V., Schmitt, A. J., Weaver, J. L., Gardner, J. H., Phillips, L., Aglitskiy, Y., Chan, Y., Dahlburg, J. P. & Klapisch, M. 2002 Effects of thin high-Z layers on the hydrodynamics of laser-accelerated plastic targets. *Phys. Plasmas* **9**, 2234-2243.
- Orlov, S. S. & Abarzhi, S. I. 2007 New experimental platform for studies of turbulence and turbulent mixing in accelerating and rotating fluids at high Reynolds numbers. *Astrophys. Space Sci.* **307**, 241-244 (2007).
- Pawley, C. J., Gerber, K., Lehmburg, R. H., McLean, E. A., Mostovych, A. N., Obenschain, S. P., Sethian, J. D., Serlin, V., Stamper, J. A., Sullivan, C. A., Bodner, S. E., Colombant, D., Dahlburg, J. P., Schmitt, A. J., Gardner, J. H., Brown, C., Seely, J. F., Lehecka, T., Aglitskiy, Y., Deniz, A. V., Chan, Y., Metzler, N. & M. Klapisch, M. 1997 Measurements of laser-imprinted perturbations and Rayleigh-Taylor growth with the Nile KrF laser. *Phys. Plasmas* **4**, 1969-1977.
- Pfalzner, S. 2006 *An Introduction to Inertial Confinement Fusion*. Taylor and Francis.
- Pikuz, S. A., Shelkovenko, T. A., Romanova, V. M., Hammer, D. A., Faenov, A. Ya., V. Dyakin, V. & Pikuz, T. A. 1995a Monochromatic x-ray probing of an ultradense plasma. *JETP Lett.* **61**, 638-644.
- Pikuz, S. A., Shelkovenko, T. A., Romanova, V. M., Hammer, D. A., Faenov, A. Ya., Dyakin, V. A. & Pikuz, T. A. 1995b High-luminosity monochromatic x-ray backlighting using incoherent plasma source to study extremely dense plasmas. In *Soft X-Ray Lasers and Applications*, J. J Rocca and P. L. Hagelstein, ed., Pros. SPIE **2520**, 330-341.

- Pikuz, S. A., Shelkovenko, T. A., Romanova, V. M., Hammer, D. A., Faenov, A. Ya., Dyakin, V. A. & Pikuz, T. A. 1997 High luminosity monochromatic x-ray backlighting using an incoherent plasma source to study extremely dense plasmas. *Rev. Sci. Instrum.* **68**, 740-744.
- Pikuz, T. A., Faenov, A. Ya., Pikuz, S. A., Romanova, V. M. & Shelkovenko, T. A. 1995 Bragg x-ray optics for imaging spectroscopy of plasma microsources. *Journal of X-ray Science and Technology* **5**, 323-340.
- Piriz, A. R., Sanz, J., and Ibañez, L. F. 1997 Rayleigh-Taylor instability of steady ablation fronts: The discontinuity model revisited. *Phys. Plasmas* **4**, 1117-1126.
- Piriz, A. R. 2001 Hydrodynamic instability of ablation fronts in inertial confinement fusion. *Phys. Plasmas* **8**, 997-1002.
- Rayleigh, L. 1883. Investigation of the character of the equilibrium of an incompressible heavy fluid of variable density, *Proc. R. Math. Soc.* **14**, 170-177.
- Regan, S. P., Marozas, J. A., Craxton R. S., Kelly J. H., Donaldson, W. R., Jaanimagi, P. A., Jacobs-Perkins, D., Keck, R. L., Kessler, T., Meyerhofer D. D., Sangster, T. C., Seka, W., Smalyuk, V. A., Skupsky, S. & Zuegel, J. D. 2005 Performance of 1-THz-bandwidth, two-dimensional smoothing by spectral dispersion and polarization smoothing of high-power, solid-state laser beams. *J. Opt. Soc. Am. B* **22**, 998-1002.
- Richtmyer, R. D. 1960 Taylor instability in shock acceleration of compressible fluids, *Commun. Pure Appl. Math.* **13**, 297-319.
- Rode, A. V., Maksimchuk, A. M., Sklizkov, G. V., Ridgley, A., Danson, C., Rizvi, N., Bann, R., Forster, E. & Uschmann, I. 1990 Intensity measurements of a quasi-monochromatic x-ray beam formed by a spherically bent crystal. *Optics Comm.* **7**, 163-166.
- Ryu, D. & Vishniac, E. T. 1987 The growth of linear perturbations of adiabatic shock waves. *Astrophys. J.* **313**, 820-841.
- Sadot, O., Levy, K., Yosel-Hai, A., Cartoon, D., Elbaz, Y., Srebro, Y., Ben-Dor, G. & Shvarts, D. 2005 Studying hydrodynamic instability using shock-tube experiments. *Astrophys. Space Sci.* **298**, 305-312.
- Sanchez del Rio, M., Faenov, A. Ya., Dyakin, V. M., Pikuz, T. A., Pikuz, S. A., Romanova, V. M. & Shelkovenko, T. A. 1997 Ray-tracing for a monochromatic x-ray backlighting scheme based on spherically bent crystal. *Physica Scripta* **55**, 735-740.
- Sanz, J. 1994 Self-consistent analytical model of the Rayleigh-Taylor instability in inertial confinement fusion. *Phys. Rev. Lett.* **73**, 2700-2703.
- Scase, M. M., Caulfield, C. P. & Dalziel, S. B. 2008 Temporal variation of non-ideal plumes with sudden reductions in buoyancy flux. *J. Fluid Mech.* **600**, 181-199.
- Schmidt, W. 2006 Turbulence - From tea kettles to exploding stars. *Nature Physics* **2**, 505-506.
- Schwaederle, L., Mariani, C., Jourdan, G., Houas, L. & Haas, J.-F. 2007 Shock-induced mixing zone characterization: an attempt by hot-wire diagnostic. *Shock Waves* **17**, 203-207.
- Sedov, L. I. 1959 *Similarity and Dimensional methods in Mechanics*. Academic.
- Shigemori, K., Nakai, M., Azechi, H., Nishihara, K., Ishizaki, R., Nagaya, T., Nagatomo, H. & Mima, K. 2000 Feed-out of rear surface perturbation due to rarefaction wave in laser-irradiated targets. *Phys. Rev. Lett.* **84**, 5331-5334.

- Smitherman, D. P., Chrien, R. E., Hoffman, N. M. & Magelssen, G. R. 1999 The feedout process: Rayleigh-Taylor and Richtmyer-Meshkov instabilities in uniform, radiation-driven foils. *Phys. Plasmas* **6**, 932-940.
- Taylor, G. I. 1950 The instability of liquid surfaces when accelerated in a direction perpendicular to their planes. *Proc. R. Soc. London A* **201**, 192-196.
- Velikovich, A. L., Dahlburg, J. P., Gardner, J. H. & Taylor, R. J. 1998 Saturation of perturbation growth in ablatively driven planar laser targets. *Phys. Plasmas* **5**, 1491-1505.
- Velikovich, A. L., Dahlburg, J. P., Schmitt, A. J., Gardner, J. H., Phillips, L., Cochran, F. L., Chong, Y. K., Dimonte, G. & Metzler, N. 2000 Richtmyer-Meshkov-like instabilities and early-time perturbation growth in laser targets and Z-pinch loads. *Phys. Plasmas* **7**, 1662-1671.
- Velikovich, A. L., Schmitt, A. J., Gardner, J. H. & Metzler, N. 2001 Feedout and Richtmyer-Meshkov instability at large density difference. *Phys. Plasmas* **8**, 592-605.
- Velikovich, A. L., Schmitt, A. J., Metzler, N. & Gardner J. H. 2003 Strong shock wave and areal mass oscillations associated with impulsive loading of planar laser targets. *Phys. Plasmas* **10**, 3270-3282.
- Velikovich, A. L., Zalesak, S. T., Metzler, N. & Wouchuk, J. G. 2005 Instability of a planar expansion wave. *Phys. Rev. E* **72**, 046306.
- Velikovich, A. L., Wouchuk, J. G., Huete Ruiz de Lira, C., Metzler, N., Zalesak, S. & Schmitt, A. J. 2007 Shock front distortion and Richtmyer-Meshkov-type growth caused by a small pre-shock non-uniformity. *Phys. Plasmas* **14**, 072706.
- Vishniac, E. T. 1983 The dynamic and gravitational instabilities of spherical shocks. *Astrophys. J.* **274**, 152-167.
- Watari, T., Nakai, M., Azechi, H., Sakaiya, T., Shiraga, H., Shigemori, K., Fujioka, S., Otani, K., Nagai, K., Sunahara, A. & Mima, K. 2008 Experimental study of density dependence of Rayleigh-Taylor instability growth. *Phys. Plasmas* **15**, 092109.
- Weaver, J. L., Chan, Y., Gardner, J., Giuliani, J., Karasik, M., Kehne, D., Mostovych, A., Obenschain, S., Velikovich, A., Schmitt, A., Serlin, V., Aglitskiy, Y., Metzler, N., Smyth, Z., Terrell, S. & Lehmborg, R. H. 2004 Short pulse experimental capability on Nike laser facility. *Bull. Am. Phys. Soc.* **49**(8), 125.
- Whitlock, R. R., Obenschain, S. P., Grun, J., Stamper, J. A., Sprague, J. A., Sweeney, B. V., Ripin, B. H. & Craxton, R. S. 1987 Flash x radiography of laser accelerated foils. *J. Appl. Phys.* **61**, 131-141.
- Wilkinson, J. P. & Jacobs, J. W. 2007 Experimental study of the single-mode three-dimensional Rayleigh-Taylor instability. *Phys. Fluids* **19**, 124102.
- Wouchuk, J. G. 2001 Growth rate of the linear Richtmyer-Meshkov instability when a shock is reflected. *Phys. Rev. E* **63**, 056303.
- Yamanaka, C. 1985 Inertial confinement fusion research by GEKKO-XII glass-laser. *Fusion Technology* **8**, 179-188.
- Zalesak, S. T., Schmitt, A. J., Gardner, J. H. & Velikovich, A. L. 2005 Modeling fluid instabilities in inertial confinement fusion hydrodynamics codes. *Phys. Plasmas* **12**, 056311.
- Zel'dovich, Ya. B. & Raizer, Yu. P. 2002 *Physics of Shock Waves and High-Temperature Hydrodynamic Phenomena* 2<sup>nd</sup> English ed. Dover.